Thin–Walled Structures 209 (2025) 112923

Contents lists available at ScienceDirect

Thin-Walled Structures

journal homepage: www.elsevier.com/locate/tws

Full length article

Structural Health Monitoring of aerospace thin plate and shell structures using the inverse finite element method (iFEM)

Ihtisham Khalid [a], Zahid Ahmed Qureshi [a], Selda Oterkus [b], Erkan Oterkus [b,*]

[a] Department of Aerospace Engineering, College of Aeronautical Engineering, National University of Sciences & Technology, Islamabad, 44000, Pakistan
[b] Department of Naval Architecture, Ocean & Marine Engineering, University of Strathclyde, Glasgow, G4 0LZ, Scotland, United Kingdom

ARTICLE INFO

Keywords:
Structural Health Monitoring
Damage assessment
Inverse problem
Shape sensing
Defects
iFEM

ABSTRACT

Thin plate and shell structures are widely used in aerospace due to their lightweight nature and efficient load-bearing capabilities, making them attractive for aircraft and spacecraft designs. This study proposes an efficient quadrilateral inverse shell element for thin structures, developed using discrete Kirchhoff assumptions, for Structural Health Monitoring (SHM) applications within the inverse finite element method (iFEM) framework. The proposed inverse formulation is straightforward, computationally efficient, and requires fewer strain sensors for full-field reconstruction than existing inverse elements based on First-Order Shear Deformation Theory (FSDT). These attributes are essential for implementing efficient SHM strategies while lowering overall project costs. The proposed inverse element is rigorously validated using benchmark problems for in-plane, out-of-plane, and general loading conditions. Its performance is compared to that of an existing competitive quadrilateral inverse shell element based on FSDT. For aerospace SHM applications, the inverse element is assessed for its shape-sensing capabilities, material discontinuity and degradation defects characterization, and structural health assessment. This research highlights the ability of the proposed inverse element to enhance SHM applications in aerospace structures, contributing to the development of more reliable and cost-effective monitoring solutions.

1. Introduction

In the aerospace sector, thin plate and shell structures are critical components that form the basis for structural designs. These lightweight and stiff structural configurations provide effective load-bearing capabilities while adhering to stringent safety standards. Ensuring the reliability and safety of airframes necessitates rigorous maintenance and inspection schedules. Traditional inspection methods, such as visual or ultrasonic testing, are effective but time-consuming, labor-intensive, and sometimes inadequate in detecting latent damages. With recent industrial revolutions, Structural Health Monitoring (SHM) has emerged as a modern tool to improve maintenance efficiency and safety. Modern SHM systems collect onboard sensory data, analyze it in real time, and predict structural behavior with greater accuracy [1]. These systems can detect damage such as cracks, delamination, or corrosion and help forecast scheduled maintenance, maximizing asset availability and safety. The most challenging and crucial aspect of a robust SHM strategy is its ability to monitor real-time structural integrity. Therefore, full-field reconstruction of displacement and stress profiles is essential. Unlike point-wise measurements, which provide data only at discrete locations, full-field reconstruction offers a comprehensive view of structural health, allowing for identifying and quantifying defects that might otherwise be missed. Developing such accurate SHM capabilities presents an inverse structural analysis problem that has intrigued researchers, as evidenced by their significant contributions to the literature.

Early research in full-field reconstruction included applying Ko's Displacement Theory [2] to reconstruct displacement profiles for airframe wing structural configurations. This methodology enables the reconstruction of wing-bending profiles with limited onboard sensors. Specifically, Ko et al. [3] relied on the assumptions of Euler Bernoulli's beam theory to reconstruct aircraft wing deflection by strategically placing strain sensors along the wing span following the main spar lines. However, the underlying assumptions limit the applicability of this methodology to capture complex structural behaviors, i.e., shear and torsional effects, making it less applicable to structures with more intricate geometry and loading conditions. Ko's methodology is primarily suited for beam-like structures, and its extension to thin shell structures may need to account for more complex deformation modes like membrane stresses or buckling. This simplification reduces its effectiveness in accurately detecting localized damage in real-world

* Corresponding author.
E-mail address: erkan.oterkus@strath.ac.uk (E. Oterkus).

https://doi.org/10.1016/j.tws.2025.112923
Received 28 October 2024; Received in revised form 27 December 2024; Accepted 6 January 2025
Available online 11 January 2025

SHM applications.

In literature, Foss et al. explored global and piecewise continuous basis functions for displacement reconstruction [4]. Similarly, Modal Transformation Theory (MTT) [5,6] received significant attention for its ability to reconstruct displacement profiles from normal mode shapes using appropriate strain–displacement relations. However, these methods depend on accurate mode shape data, which can be influenced by material degradation or structural damage. Also, these methods rely on limited modes for reconstructing displacement profiles, potentially overlooking complex or localized deformation behavior crucial to SHM applications. Later, Shkarayev et al. [7] introduced a two-step least squares method for displacement reconstruction. This approach estimates the applied load on the structure in the first step, followed by determining the displacement field in the second step. As a result, the reliability of the reconstructed displacements depends heavily on the accuracy of the load predictions. Consequently, even minor errors in load estimations can lead to significant inaccuracies in the reconstructed displacement profiles.

Recently, researchers have employed variational approaches to model-based formulations to develop full-field displacement reconstruction capabilities. Tessler and Spangler [8] proposed the Inverse Finite Element Method (iFEM) framework by developing a variational error functional utilizing on-board discrete strain data and numerical strain approximations from the Finite Element Method (FEM) to reconstruct displacement profiles. A key advantage of the iFEM framework is its independence from constitutive relations and loading conditions. Consequently, the iFEM framework can reconstruct full-field displacements relying solely on boundary conditions. The iFEM framework is also robust enough to handle sparse strain measures in reliably reconstructing displacement fields. These capabilities are valuable in contrast to traditional methods necessitating precise material properties and loading information, enabling more effective identification and quantification of structural defects.

Similarly, data-driven approaches [9,10] based on Deep Neural Networks (DNN) offer substantial benefits in reconstructing complex structural behavior. These data-based frameworks are robust and capable of handling forward and inverse analysis, making them highly suitable for SHM applications. However, these methods are data-intensive, mandating substantial computational power and an entirely different machine learning (ML) framework for implementation [11]. Despite these challenges, DNN-based methods present promising alternatives for SHM applications, particularly when traditional physics-based approaches face limitations in capturing intricate structural responses [1].

The framework of iFEM has emerged as an effective tool for full-field reconstruction and SHM applications, offering the potential for real-time damage assessment of various engineering structures. Researchers have proposed various inverse elements tailored to specific structural configurations, highlighting the versatility of iFEM in advancing Structural Health Monitoring (SHM). Tessler and Spangler. [12] developed a three-node triangular inverse element (iMIN3) to demonstrate the capability of the iFEM framework for full-field shape-sensing applications. A four-node quadrilateral inverse shell element (iQS4) was introduced by Kefal et al. [13] for SHM applications in the naval sector. Later, they developed curved quadrilateral inverse shell elements (iCS8) to improve SHM capabilities in marine and offshore structures [14]. Khalid et al. [15] developed iKP4 inverse plate element using non-conforming Hermite basis functions for shape-sensing applications of thin plate structures. Similarly, isogeometric inverse elements iKLS and IgaiMin were developed to analyze geometrically complex structures [16–18]. These higher-order elements enhance interelement compatibility and help seamless integration with geometric modeling. A three-dimensional solid inverse element was presented by De Mooij et al. [19] to extend the application of iFEM in analyzing thick structures. Recent studies have advanced deformation reconstruction and shape sensing using nonlinear iFEM algorithms, quasi-3D zigzag beam theory, and full-field iFEM for thin-walled structures [20–22]. Based on the Refined Zigzag theory, a three-node inverse element (i3-RZT) was proposed to extend the iFEM capabilities to composite laminates and sandwich structures [23]. Khalid et al. recently introduced an inverse crack tip element (iTP6) to perform iFEM analysis on structures with preexisting cracks and reconstruct crack mechanics [24].

Various inverse elements in the literature are based on First-Order Shear Deformation Theory (FSDT), which is used to undertake iFEM analysis of thin and thick shell structures. In dealing with thicker structures, shear correction factors are employed, and transverse shear strains are computed using FSDT equilibrium equations. In contrast, in dealing with thin structures, the transverse shear effects are neglected; however, this assumption does not simplify the overall inverse formulation to capitalize on computational efficiency. One of the challenges associated with FSDT-based elements is shear locking when dealing with thin structures because of the excessive influence of the transverse shear deformation terms. Furthermore, these elements exhibit slow convergence when applied to thin plate and shell structures, requiring a significantly large number of onboard strain sensors. As a result, FSDT-based inverse elements often face challenges in accurately analyzing thin structures due to high computational costs and the need for an impractically large number of onboard sensors. The literature highlights that the effectiveness of iFEM analysis is highly dependent on the underlying kinematics integrated into the inverse formulation. Therefore, there is a need for an inverse formulation explicitly designed for thin shell structures, which helps to optimize computational efficiency and minimize sensor requirements. These features are crucial for SHM applications, where real-time monitoring and precise damage detection are vital for maintaining structural integrity and safety.

This study aims to overcome some limitations of existing FSDT-based inverse formulations in dealing with thin shell structures by proposing a new quadrilateral inverse shell element (iKS4) for SHM applications. The proposed inverse shell formulation is straightforward, neglecting transverse shear effects using discrete Kirchhoff assumptions. Hierarchical drilling rotation is incorporated to enhance element compatibility and extend the practical usefulness of iKS4 to access built-up structures. Unlike existing FSDT-based elements, the proposed inverse element is simple in its formulation, computationally efficient, and free from shear-locking issues in dealing with thin plate and shell structures. A rigorous numerical validation study evaluates the performance of the newly proposed inverse formulation using famous benchmark problems. A comparative analysis of the proposed inverse formulation is performed against an existing iQS4 inverse shell element to assess its accuracy and efficiency in reconstructing the displacement field. In the context of SHM applications, the iKS4 inverse shell element is numerically evaluated by considering an aircraft fuselage stiffened panel subjected to cabin pressurization conditions. Furthermore, the inverse formulation is evaluated for its defect detection capabilities by considering two common categories in the aerospace industry: geometric discontinuities, such as voids, cracks, and material degradations resulting from cyclic loading.

The rest of the article is organized as follows. Inverse shell formulation and theoretical insights are presented in Section 2. To focus on key mathematical steps, shape functions for quadrilateral element, drilling rotation DOF, and discrete Kirchhoff bending field are outlined in Appendices A.1, A.2, A.3. The details about the coordinate transformation system essential for shell formulations are explained in Appendix A.4. Section 3 offers numerical validation through benchmark results and a standardized analysis setup to compare iFEM results from iKS4 and iQS4 inverse elements. Real-world SHM applications, including displacement reconstruction and defect identification, are examined in Section 4. Finally, the conclusion summarizes the findings in light of the detailed analysis and discussion of the numerical cases considered in the study.

2. Formulation of inverse shell element

According to the kinematics of Classical Plate Theory (CPT), Kirchhoff-based elements require the deflection field to have C^1 continuity because of the presence of second derivatives of the deflection in the virtual work expression. Achieving C^1 continuity generally requires special techniques like using Hermite basis functions, which increases computational complexity and makes it challenging to analyze built-up structures [25].

Batoz et al. [26] introduced the Discrete Kirchhoff Theory to circumvent the strict continuity requirement by imposing the Kirchhoff hypothesis only along the edges of the element to relate the rotations to the transverse displacements. This approach allows simpler C^0 continuity elements while still ensuring that the solution converges to the Kirchhoff plate theory solution. The formulation is based upon the discretization of strain energy where transverse shear energy is neglected, consistent with the thin plate theory assumptions. The independent bending variables in this formulation are the deflection w and the rotations $(\theta_x), \theta_y$ requiring only C^0 continuity. The Kirchhoff hypothesis is discretely applied along the element edges to relate rotations to transverse displacements, such that $\theta_x = -w_{,y}$ and $\theta_y = w_{,x}$.

A general expression for the strain field with membrane and bending components can be written as:

$$\boldsymbol{\varepsilon}(\mathbf{u}) = \boldsymbol{e}(\mathbf{u}) + \boldsymbol{\kappa}(\mathbf{u}) \tag{1}$$

where, $\boldsymbol{\varepsilon}(\mathbf{u})$ is the strain field defined in terms of the displacement field $\mathbf{u}(x, y)$. The component $\boldsymbol{e}(\mathbf{u})$ represents the membrane strains, and $\boldsymbol{\kappa}(\mathbf{u})$ denotes the bending strains associated with bending curvatures. The strain field can be further expressed in terms of strain components as:

$$\boldsymbol{\varepsilon}(\mathbf{u}) = \begin{Bmatrix} \varepsilon_{xx} \\ \varepsilon_{yy} \\ \gamma_{xy} \end{Bmatrix} = \begin{Bmatrix} \varepsilon^o_{xx} \\ \varepsilon^o_{yy} \\ \gamma^o_{xy} \end{Bmatrix} - z \begin{Bmatrix} \kappa_{xx} \\ \kappa_{yy} \\ \kappa_{xy} \end{Bmatrix} \tag{2}$$

where membrane and bending curvatures can be written more conveniently as:

$$\boldsymbol{e}(\mathbf{u}) = \begin{Bmatrix} \varepsilon^o_{xx} \\ \varepsilon^o_{yy} \\ \gamma^o_{xy} \end{Bmatrix} = \begin{bmatrix} \frac{\partial}{\partial x} & 0 \\ 0 & \frac{\partial}{\partial y} \\ \frac{\partial}{\partial y} & \frac{\partial}{\partial x} \end{bmatrix} \begin{Bmatrix} u_o \\ v_o \end{Bmatrix} \tag{3}$$

$$\boldsymbol{\kappa}(\mathbf{u}) = \begin{Bmatrix} \kappa_{xx} \\ \kappa_{yy} \\ \kappa_{xy} \end{Bmatrix} = \begin{bmatrix} \frac{\partial}{\partial x} & 0 \\ 0 & \frac{\partial}{\partial y} \\ \frac{\partial}{\partial y} & \frac{\partial}{\partial x} \end{bmatrix} \begin{Bmatrix} \theta_x \\ \theta_y \end{Bmatrix} \tag{4}$$

The independent rotations θ_x and θ_y are related to the nodal displacement in such a way that the final element retains the characteristics of a Kirchhoff-type element. These strain–displacement relationships are subsequently used in inverse shell formulation based on iFEM weighted least-squares functional.

The constitutive relationship between non-zero stress and strain states can be established for a material exhibiting homogeneity and subjected to isothermal conditions as

$$\boldsymbol{\sigma}(\mathbf{u}) = [\boldsymbol{C}]\boldsymbol{\varepsilon}(\mathbf{u}) \tag{5}$$

where $\boldsymbol{C}$ is the constitutive matrix containing the material properties. Due to the thin plate theory assumptions, the transverse normal and transverse shear stresses ($\sigma_{zz} = \gamma_{yz} = \gamma_{xz} = 0$) are zero. The constitutive matrices $\boldsymbol{C}$ for an isotropic material can be expressed as follows:

$$\boldsymbol{C} = \frac{E}{(1-\nu^2)} \begin{bmatrix} 1 & -\nu & 0 \\ -\nu & 1 & 0 \\ 0 & 0 & \frac{1-\nu}{2} \end{bmatrix} \tag{6}$$

where E and ν represent Young's modulus of elasticity and Poisson's ratio.

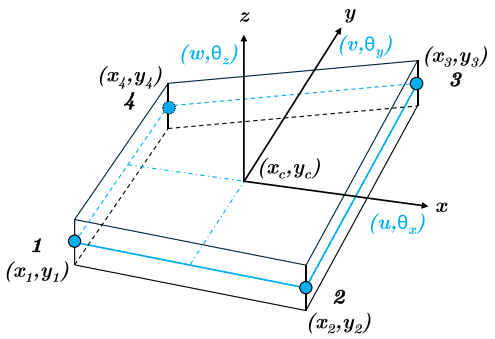

Fig. 1. iKS4 Defined in the Physical Coordinate System.

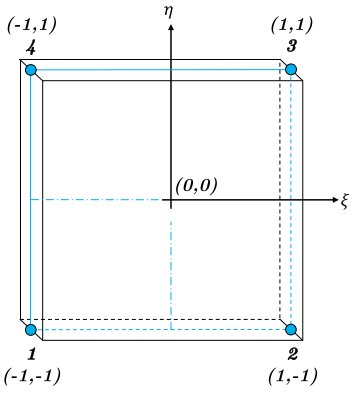

Fig. 2. Master element defined in natural coordinate system.

To start with finite element approximation, consider a four-node quadrilateral inverse shell element defined in the physical coordinate system (x, y, z) with nodes located at the mid-plane, where $z \in [-t/2, t/2]$ defines the thickness of the element as shown in Fig. 1. The master element depicted in Fig. 2 is defined in the natural coordinate system (ξ, η).

The geometrical mapping between physical and natural coordinate systems is achieved using isoparametric bi-linear basis functions $N_i(\xi, \eta)$ expressed as follows:

$$N_i = \frac{1}{4}\left(1 + \xi_o\right)\left(1 + \eta_o\right) \tag{7}$$

$$\xi_o = \xi\xi_i, \quad \eta_o = \eta\eta_i \quad (i = 1, 2, 3, 4)$$

where ξ_i and η_i denote natural coordinates of the i^{th} node of the element, and the explicit form of isoparametric bi-linear basis functions is provided in Appendix A.1.

In shell formulations, 6 degrees of freedom (DOF) per node are often considered, including three displacements and rotations at each node. The nodal displacement vector for the iKS4 inverse shell element is written as:

$$\mathbf{u}^e_i = \begin{bmatrix} (u_o)_i \\ (v_o)_i \\ (w)_i \\ (\theta_x)_i \\ (\theta_y)_i \\ (\theta_z)_i \end{bmatrix} \quad (i = 1, 2, 3, 4) \tag{8}$$

For the ith node of inverse element, (u_o, v_o, w) are the nodal displacements, while (θ_x, θ_y) correspond to the bending rotations along y and x axis, respectively. The variable θ_z denotes drilling rotation, which is hierarchical in nature. Allman [27] originally introduced the concept of drilling degrees of freedom (DOFs) to improve element compatibility.

Furthermore, drilling DOF rotation helps to prevent coplanar singularity issues when dealing with complex built-up structures. During iFEM shape sensing analysis, these unknown nodal displacements are reconstructed using onboard discrete strain measures.

The in-plane translational displacement variables u and v can be expressed using isoparametric bi-linear basis functions expressed in the Eq. (7) as

$$u = \sum_{i=1}^{4} N_i(\xi,\eta)u_{o_i} + \sum_{i=1}^{4} L_i(\xi,\eta)\theta_{z_i} \tag{9}$$

$$v = \sum_{i=1}^{4} N_i(\xi,\eta)v_{o_i} + \sum_{i=1}^{4} M_i(\xi,\eta)\theta_{z_i} \tag{10}$$

where $L(\xi,\eta)$ and $M(\xi,\eta)$ are anisoparametric shape functions, and their explicit expressions are provided in Appendix A.2. Incorporating drilling rotation DOF θ_z extends the conventional in-plane kinematics to represent the element behavior comprehensively.

The membrane nodal variables vector $\mathbf{u}_i^m$, which includes both displacements and drilling rotation, is expressed as:

$$\mathbf{u}_i^m = \begin{bmatrix} (u_o)_i \\ (v_o)_i \\ (\theta_z)_i \end{bmatrix} (i = 1,2,3,4), \quad \mathbf{u}^m = \begin{bmatrix} \mathbf{u}_1^m \\ \mathbf{u}_2^m \\ \mathbf{u}_3^m \\ \mathbf{u}_4^m \end{bmatrix} \tag{11}$$

where $\mathbf{u}^m$ represents the complete membrane displacement field for the inverse element. Numerical elemental strains $\boldsymbol{e}(\mathbf{u}^e)$ for the membrane part of the formulation can be computed using Eqs. (9) and (10) in Eq. (3).

$$\boldsymbol{e}(\mathbf{u}^e) = \boldsymbol{B}^m\mathbf{u}^e \tag{12}$$

where $\boldsymbol{B}^m$ represents the membrane gradient matrix of the element and $\mathbf{u}^e$ is the displacement vector. The nodal membrane gradient matrix $\boldsymbol{B}_i^m$ can be expressed in terms of the nodal basis functions as:

$$\boldsymbol{B}_i^m = \begin{bmatrix} \frac{\partial N_i}{\partial x} & 0 & 0 & 0 & 0 & \frac{\partial L_i}{\partial x} \\ 0 & \frac{\partial N_i}{\partial y} & 0 & 0 & 0 & \frac{\partial M_i}{\partial y} \\ \frac{\partial N_i}{\partial y} & \frac{\partial N_i}{\partial x} & 0 & 0 & 0 & \frac{\partial M_i}{\partial x} + \frac{\partial L_i}{\partial y} \end{bmatrix} \tag{13}$$

By assembling the nodal gradient matrices $\boldsymbol{B}_i^m$ for each node ($i = 1,2,3,4$), the membrane gradient matrix $\boldsymbol{B}^m$ for the complete element is computed as:

$$\boldsymbol{B}^m = \begin{bmatrix} \boldsymbol{B}_1^m & \boldsymbol{B}_2^m & \boldsymbol{B}_3^m & \boldsymbol{B}_4^m \end{bmatrix} \tag{14}$$

The formulation of the bending gradient matrix is derived from the Discrete Kirchhoff Quadrilateral (DKQ) bending element, as originally developed by Batoz et al. [26]. While the detailed derivation of the DKQ bending element is well-documented in the existing literature; this discussion focuses on utilizing its displacement field to formulate the bending gradient matrix for the current inverse shell element.

In a bi-linear domain, the independent bending rotations θ_x and θ_y can be approximated using anisoparametric shape functions based on the discrete Kirchhoff hypothesis.

$$\theta_x = \boldsymbol{H}^x(\xi,\eta)^{\mathrm{T}}\mathbf{u}^b \tag{15}$$

$$\theta_y = \boldsymbol{H}^y(\xi,\eta)^{\mathrm{T}}\mathbf{u}^b \tag{16}$$

Here, $\boldsymbol{H}^x(\xi,\eta)$ and $\boldsymbol{H}^y(\xi,\eta)$ are the shape function vectors mapping the element displacement field $\mathbf{u}^b$ to the independent bending rotations θ_x and θ_y, respectively. Both $\boldsymbol{H}^x(\xi,\eta)$ and $\boldsymbol{H}^y(\xi,\eta)$ comprise twelve anisoparametric shape functions introduced by Batoz et al. [26], defined using the standard quadratic basis functions of the eight-node quadrilateral element (provided in Appendix A.1). The explicit expressions for $(\boldsymbol{H}^x, \boldsymbol{H}^y)$ shape function vectors are provided in Appendix A.3.

The bending nodal variables $\mathbf{u}_i^b$ can be assembled to formulate an element's bending displacement field $\mathbf{u}_i^b$ as follows:

$$\mathbf{u}_i^b = \begin{bmatrix} (w)_i \\ (\theta_x)_i \\ (\theta_y)_i \end{bmatrix} (i = 1,2,3,4), \quad \mathbf{u}^b = \begin{bmatrix} \mathbf{u}_1^b \\ \mathbf{u}_2^b \\ \mathbf{u}_3^b \\ \mathbf{u}_4^b \end{bmatrix} \tag{17}$$

Like the membrane part, numerical elemental strains $\boldsymbol{\kappa}(\mathbf{u}^e)$ for the bending part can be computed using Eqs. (15) and (16) in Eq. (4).

$$\boldsymbol{\kappa}(\mathbf{u}^e) = \boldsymbol{B}^b\mathbf{u}^e \tag{18}$$

where $\boldsymbol{B}^b$ represents the element bending gradient matrix. The nodal bending gradient matrix $\boldsymbol{B}_i^b$ can be written in terms of $\boldsymbol{H}^x$ and $\boldsymbol{H}^y$ shape functions as:

$$\boldsymbol{B}_i^b = \begin{bmatrix} 0 & 0 & \boldsymbol{H}^x_{j+1,x} & \boldsymbol{H}^x_{j+2,x} & \boldsymbol{H}^x_{j+3,x} & 0 \\ 0 & 0 & \boldsymbol{H}^y_{j+1,y} & \boldsymbol{H}^y_{j+2,y} & \boldsymbol{H}^y_{j+3,y} & 0 \\ 0 & 0 & \boldsymbol{H}^y_{j+1,x} + \boldsymbol{H}^x_{j+1,y} & \boldsymbol{H}^y_{j+2,x} + \boldsymbol{H}^x_{j+2,y} & \boldsymbol{H}^y_{j+3,x} + \boldsymbol{H}^x_{j+3,y} & 0 \end{bmatrix} \tag{19}$$

$$where j = 3(i-1), \quad for i = 1,2,3,4$$

The bending gradient matrix $\boldsymbol{B}^b$ can be formulated by concatenating $\boldsymbol{B}_i^b$ for each node ($i = 1,2,3,4$) of the iKS4 inverse shell element as:

$$\boldsymbol{B}^b = \begin{bmatrix} \boldsymbol{B}_1^b & \boldsymbol{B}_2^b & \boldsymbol{B}_3^b & \boldsymbol{B}_4^b \end{bmatrix} \tag{20}$$

The iFEM framework is built on the principle of the variational method, where the displacement field is reconstructed by minimizing the weighted least squares error functional. The error functional is formulated using discrete strain measures and their corresponding numerical counterparts in a discretized geometric space. One of the significant benefits of the iFEM scheme is its independence from elastic or inertial material properties and loading conditions for full-field shape reconstruction.

The weighted least squares functional for the proposed iKS4 element is defined as the sum of the error terms between the numerical and discretely measured values of the membrane and bending strains as

$$\boldsymbol{\phi}^e(\mathbf{u}^e) = w_e \left\|\boldsymbol{e}(\mathbf{u}^e) - \boldsymbol{e}^*\right\|^2 + w_k \left\|\boldsymbol{\kappa}(\mathbf{u}^e) - \boldsymbol{\kappa}^*\right\|^2 \tag{21}$$

where $\boldsymbol{e}(\mathbf{u}^e)$ and $\boldsymbol{\kappa}(\mathbf{u}^e)$ represent numerically computed elemental membrane and bending strains. In contrast, $\boldsymbol{e}^*$ and $\boldsymbol{\kappa}^*$ indicate in-situ discrete strain measures obtained from the strain sensors located in the discretized elemental geometric domains; w_e and w_k are the weighting coefficients associated with the squared norms corresponding to membrane and bending errors, respectively. Each of the squared norms defined in Eq. (21) can be further expressed over the inverse element domain Ω^{iel} as:

$$\left\|\boldsymbol{e}(\mathbf{u}^e) - \boldsymbol{e}^*\right\|^2 = \iint_{A_e} \left(\boldsymbol{e}(\mathbf{u}^e) - \boldsymbol{e}^*\right)^2 \mathrm{dxdy} \tag{22}$$

$$\left\|\boldsymbol{\kappa}(\mathbf{u}^e) - \boldsymbol{\kappa}^*\right\|^2 = t^2 \iint_{A_e} \left(\boldsymbol{\kappa}(\mathbf{u}^e) - \boldsymbol{\kappa}^*\right)^2 \mathrm{dxdy} \tag{23}$$

where A_e represents the area of an inverse element.

Discrete strain sensor measurements play a crucial role in the iFEM formulation, which are measured discretely (x_j, y_j) at the mid-plane of the shell, as shown in Fig. 3. For complex built-up structures and general loading conditions, strain sensors are needed on both surfaces of the structure for accurate computation of the section strains. However, strain data from either surface (top or bottom) suffices for iFEM analysis of specific cases, such as plane stress or pure bending. The in-situ strain data usually obtained from the onboard strain sensors can be represented as discrete measurements of membrane and bending

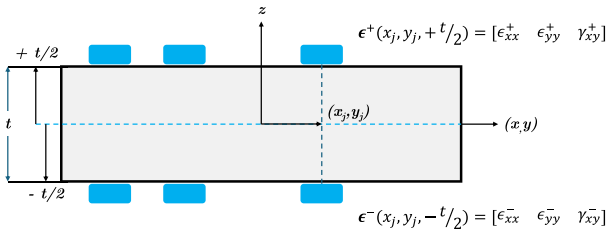

Fig. 3. Strain rosettes at discrete locations $(x_j, y_j, \pm\frac{t}{2})$.

strains:

$$\boldsymbol{e}^* = \frac{1}{2}\begin{Bmatrix} \epsilon^+_{xx} + \epsilon^-_{xx} \\ \epsilon^+_{yy} + \epsilon^-_{yy} \\ \gamma^+_{xy} + \gamma^-_{xy} \end{Bmatrix} \tag{24}$$

$$\boldsymbol{\kappa}^* = \frac{1}{t}\begin{Bmatrix} \epsilon^+_{xx} - \epsilon^-_{xx} \\ \epsilon^+_{yy} - \epsilon^-_{yy} \\ \gamma^+_{xy} - \gamma^-_{xy} \end{Bmatrix} \tag{25}$$

where $\boldsymbol{e}^*$ and $\boldsymbol{\kappa}^*$ are the discrete strain measures defined at location (x_j, y_j) within the spatial domain of an inverse element. The superscripts (+) and (−) refer to strain measurements obtained from the strain rosettes installed on the top and bottom surfaces of the shell structure, respectively.

The weighting coefficients w_e and w_k, defined in the least squares error functional in Eq. (21), are chosen based on the availability of discrete strain measures for the given inverse element. If discrete strain measures ($\boldsymbol{e}^*$, $\boldsymbol{\kappa}^*$) are available within the spatial domain of the inverse element, the coefficients can be set to unity, $w_e = w_k = 1$. Otherwise, if strain measures are missing within an inverse element, the coefficients are set to minimal values $(w_e, w_k) \ll 1$. During the least squares error minimization process, these weighting coefficients help to balance the influence of available discrete strain measures in the closed-form solution. Setting the coefficients to unity ($w_e = w_k = 1$) gives equal importance to all data points, which are known with certainty when the strain measures are available. On the other hand, setting the coefficients to a minimal value ($w_e = w_k = 10^{-3} to 10^{-6}$) when the strain data is missing reduces the impact of these missing data points during the error minimization process, preventing them from unduly affecting the overall result. This approach helps to ensure that the iFEM algorithm exhibits its intended robustness for real-world SHM applications.

Minimizing the weighted least squares error functional in Eq. (21) with respect to the unknown nodal displacements $\mathbf{u}^e$ of an inverse element reduces to the conventional system of the linear equations:

$$\frac{\partial \boldsymbol{\phi}^e(\mathbf{u}^e)}{\partial \mathbf{u}^e} = \boldsymbol{m}^e\mathbf{u}^e - \boldsymbol{s}^e = 0 \tag{26}$$

The equilibrium equations can thus be written as:

$$\boldsymbol{m}^e\mathbf{u}^e = \boldsymbol{s}^e \tag{27}$$

where $\boldsymbol{m}^e$ represents the error minimization matrix, $\boldsymbol{s}^e$ is the measured strain vector comprising discrete strain measures obtained from the onboard strain sensors, and $\mathbf{u}^e$ is the unknown nodal displacements to be determined after prescribing necessary displacement boundary conditions. The mathematical expressions representing $\boldsymbol{m}^e$ and $\boldsymbol{s}^e$ can be written as:

$$\boldsymbol{m}^e = \iint_{A_e} \left(w_e(\boldsymbol{B}^m)^{\mathrm{T}}\boldsymbol{B}^m + (t^2)w_k(\boldsymbol{B}^b)^{\mathrm{T}}\boldsymbol{B}^b \right) \mathrm{dxdy} \tag{28}$$

$$\boldsymbol{s}^e = \iint_{A_e} \left(w_e(\boldsymbol{B}^m)^{\mathrm{T}}\boldsymbol{e}^* + (t^2)w_k(\boldsymbol{B}^b)^{\mathrm{T}}\boldsymbol{\kappa}^* \right) \mathrm{dxdy} \tag{29}$$

Next, the global system of equations can be formulated based on the element contributions given in Eqs. (28) and (29) as:

$$\boldsymbol{M}\mathbf{U} = \boldsymbol{S} \tag{30}$$

where $\boldsymbol{M}$ is the global error minimization matrix, $\mathbf{U}$ is the global unknown displacement vector, and $\boldsymbol{S}$ is the global measured strain vector. These global matrices are derived by summing the transformed element-level quantities using the element transformation matrix $\boldsymbol{T}^e$.

$$\boldsymbol{M} = \sum_{e=1}^{N_{iel}} \boldsymbol{T}^{e\mathrm{T}}(\boldsymbol{m}^e)\boldsymbol{T}^e \tag{31}$$

$$\mathbf{U} = \sum_{e=1}^{N_{iel}} \boldsymbol{T}^{e\mathrm{T}}(\mathbf{u}^e) \tag{32}$$

$$\boldsymbol{S} = \sum_{e=1}^{N_{iel}} \boldsymbol{T}^{e\mathrm{T}}(\boldsymbol{s}^e) \tag{33}$$

where N_{iel} denotes the total number of inverse elements in the spatial domain. The element transformation matrix $\boldsymbol{T}^e$ ensures the transformation of the element-level matrices ($\boldsymbol{m}^e$, $\mathbf{u}^e$, and $\boldsymbol{s}^e$) to the global coordinate system before their assembly. The detailed methodology to obtain the element transformation matrix is presented in Appendix A.4.

After prescribing the essential boundary conditions, the partitioned global system of equations can be written as:

$$\boldsymbol{M}_p\mathbf{U}_p = \boldsymbol{S}_p \tag{34}$$

Consequently, $\boldsymbol{M}_p$, $\mathbf{U}_p$, and $\boldsymbol{S}_p$ imply the partitioned global system of equilibrium equations in the iFEM formulation. The unknown nodal displacements can be computed by solving these equations to reconstruct full-field displacement profiles.

3. Numerical validation

The validation of the inverse formulation requires discrete strain data. This data can be obtained in two ways. Experimental strain data is collected using strain gauges on the structural system. On the other hand, synthetic strain data can be obtained through high-fidelity forward FEM analysis. Under similar loading and boundary conditions, the strain data acquired through FEM analysis can reliably duplicate the experimental strain data obtained from the experimental setup. Since FEM is a well-established analysis technique, the numerical validation of inverse formulations via synthetic strain data is widely accepted in the engineering community as a reliable validation methodology. As reported in the literature, a similar validation methodology has been widely used in formulating inverse elements [13,17,28].

The iFEM formulation of the iKS4 inverse shell element is numerically validated, considering famous benchmark problems from the existing literature. A rigorous numerical validation plan includes evaluating the iKS4 inverse element under in-plane (membrane), out-of-plane (bending), and general loading for curved shell structures. Numerical modeling is widely employed in research and development to simulate real-world phenomena. Since numerical models, such as iFEM, rely on various assumptions and simplifications, validating them against analytical solutions is essential to confirm their accuracy and reliability for real-world applications. However, when analytical solutions are not available for complex cases, the high-fidelity FEM reference solutions allow for the reliable comparison of iFEM results.

The numerical cases considered in this section serve two essential purposes: first, to validate the iKS4 inverse shell element, and second, to compare its performance with the existing iQS4 inverse shell element [13]. In both cases, shear deformation effects are neglected when analyzing thin plate and shell structures, aligning with the mechanics of these problems. Kefal et al. [13] previously recommended this assumption for implementing the iQS4 inverse element in thin shell structures. However, in the iKS4 inverse formulation, the exclusion of shear deformation is inherent, as it is based on Classical Plate Theory (CPT). The absence of shear deformation terms in the proposed iKS4 inverse formulation simplifies the weighted least squares error functional in iFEM analysis. In contrast, the iQS4 formulation, based on FSDT assumptions, requires the computation of numerical transverse

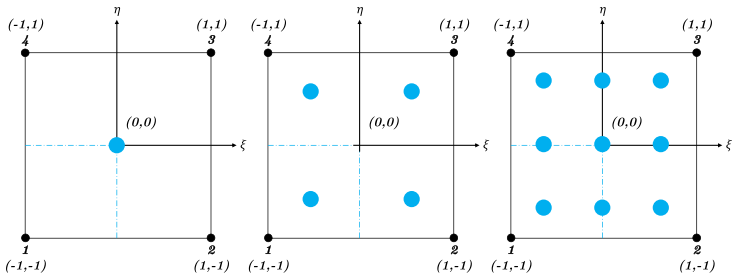

Fig. 4. 1, 2, and 3 Point Gauss locations in master element.

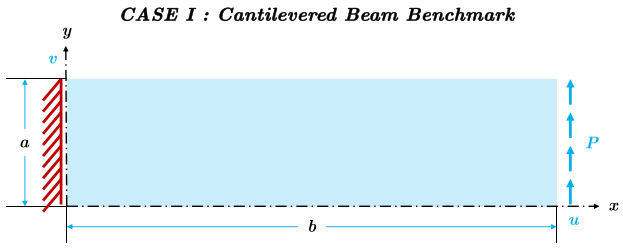

Fig. 5. Cantilevered beam — free edge under shear load.

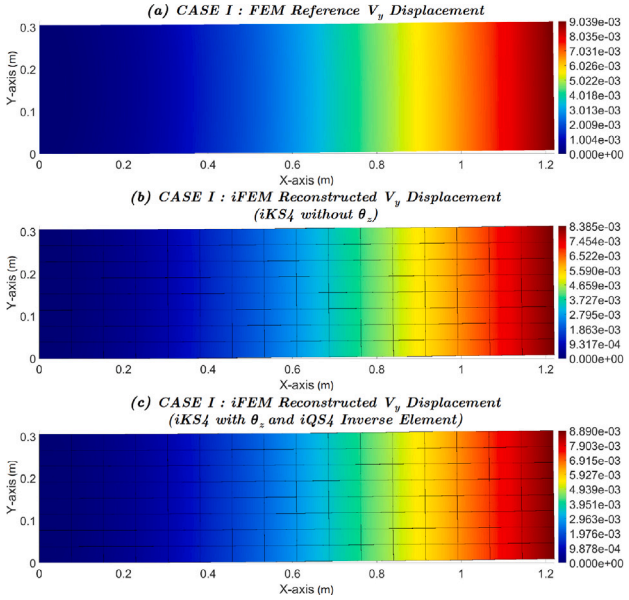

Fig. 6. Case I - Vertical displacement profiles: (a) FEM^{Ref}, (b) iFEM iKS4, and (c) iFEM iQS4.

shear strains due to the inclusion of shear deformation terms. Even when the shear deformation effects are neglected in the iQS4 element, it does not provide the same computational advantage as the iKS4 inverse formulation, which inherently benefits from excluding these terms and necessitates fewer onboard sensors.

In iFEM applications, two sensor arrangements are typically employed during the numerical validation: dense and sparse configurations. Dense sensor arrangements are used to assess the accuracy of iFEM formulations, providing discrete strain data to all inverse elements for precise validation. In contrast, Sparse sensor arrangements provide strain measures for fewer inverse elements to evaluate the robustness of the iFEM algorithm, simulating its performance under real-world practicable onboard sensor arrangements. To ensure an intuitive and accurate comparison, the numerical validation of iKS4 and iQS4 inverse shell elements is conducted under a standardized dense sensor arrangement. Another factor influencing the accuracy of iFEM analysis is the strain rosette's location within the inverse element domain.

In iFEM analysis, the strain rosette can be placed at various locations within the inverse element domain, including commonly used positions like Gauss points, as illustrated in Fig. 4. The choice of discrete locations can be optimized based on factors such as the geometric configuration of the engineering structure, loading conditions, and critical stress areas. For this study, the strain rosette is consistently placed at the center of the inverse element domain (single point Gauss location) for all numerical validation cases under consideration.

3.1. In-plane loading (Case - I)

The plane stress condition represents one of the simplest cases in two-dimensional structural analysis. Analytical solutions exist for various problems involving point loads and edge tractions. Several studies [29,30] have employed shear-loaded cantilever beams to assess the membrane behavior of newly developed elements. In this work, we revisit this problem to evaluate the membrane response capabilities of the newly formulated iKS4 inverse shell element.

A rectangular beam with dimensions $b = 1.2192$ m (length), $a = 0.3048$ m (width), and a constant cross-sectional thickness of $t = 25.4$ mm, is considered. The left edge is fixed, while the right edge is subjected to a resultant shear load of $P = 177.929$ kN, as illustrated in Fig. 5. The beam material is homogeneous and isotropic, with an elastic modulus $E = 206.84$ GPa and Poisson's ratio $\nu = 0.25$. According to the elasticity solution by Timoshenko [31], the maximum vertical displacement at the tip of the free edge is given as:

$$V = \frac{4Pa^3}{Etb^3} + \frac{2(4+5\nu)Pa}{4Etb} = 9.025 \text{ mm} \tag{35}$$

A high-fidelity FEM analysis is conducted to solve the cantilevered beam benchmark problem. The maximum vertical displacement obtained from the forward FEM analysis is 9.039 mm (as shown in Fig. 6a), which conforms well with the analytical solution. The displacement field from the high-fidelity FEM solution is used to generate synthetic discrete strain measures at the centroids of the inverse elements. These discrete strain measures are utilized in the iFEM analysis using the proposed inverse formulation and the iQS4 inverse element. For membrane problems, strain sensors on either side of the beam generate the required strain data, as the displacement field remains constant through the thickness under in-plane loading conditions.

The iFEM analysis uses two configurations of the iKS4 inverse shell element: one configuration neglects the drilling rotation (θ_z) degrees of freedom (DOF), given that drilling rotations are hierarchical and can be omitted during analysis. In contrast, the other configuration includes the drilling rotation (θ_z). This approach offers a detailed insight into the impact and significance of drilling rotations on the performance of the iKS4 inverse shell element.

The reconstructed vertical displacement profiles for the 16×8 inverse discretization are shown in Figs. 6b and 6c for the iKS4 inverse

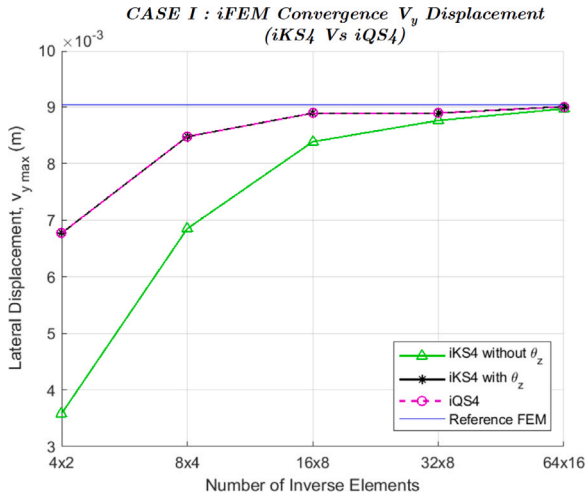

Fig. 7. Case I - Influence of inverse discretization on reconstructed vertical displacement.

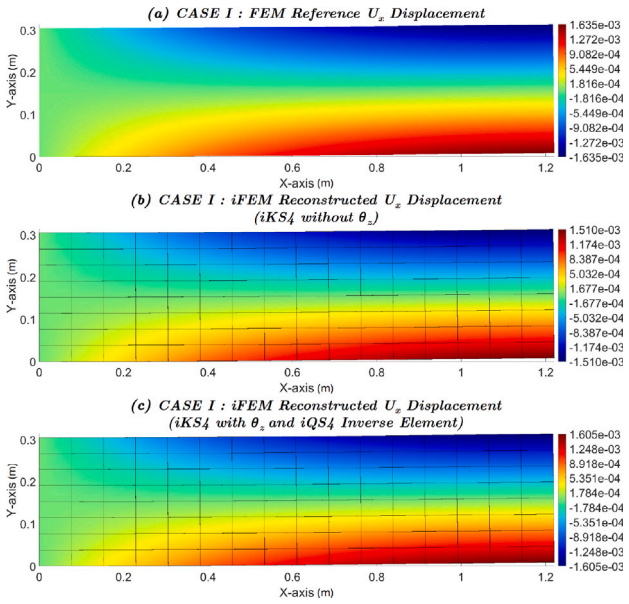

Fig. 8. Case I - Horizontal displacement profiles: (a) FEM^{Ref}, (b) iFEM iKS4, and (c) iFEM iQS4.

element, omitting drilling rotations in the former and including them in the latter. Since the membrane formulation is the same for the iKS4 and iQS4 inverse shell elements, their reconstructed displacement profiles are consequently similar. The absolute error in the reconstruction of the maximum vertical displacement, compared to the analytical solution (Eq. (35)), is 7.09% when drilling rotations are omitted and reduces to 1.49% when drilling rotations are included. However, the reconstructed displacement contours for both configurations are virtually indistinguishable as compared to the high-fidelity FEM reference solution shown in Figs. 6a.

Fig. 7 illustrates the influence of inverse discretization on the reconstruction of the vertical displacement profile. The convergence plot demonstrates the monotonic convergence of the reconstructed displacements for both configurations of the iKS4 inverse element (with and without drilling rotation DOF) and the iQS4 inverse element as the number of inverse elements increases. The enhanced membrane response capability of iKS4 and iQS4 inverse shell elements is due to hierarchical drilling rotation, which improves their ability to capture in-plane rotational effects, resulting in more accurate membrane behavior and faster convergence. Without drilling rotation DOF, the iFEM results slowly converge to the elasticity solution using more inverse elements, consequently necessitating more onboard strain sensors.

The high-fidelity FEM reference solution in Fig. 8a shows the maximum horizontal displacement of 1.635 mm. Reconstructed horizontal displacement contours of iKS4 (with and without drilling rotation DOF) and iQS4 inverse elements are in close agreement with the high-fidelity FEM reference solution, as shown in Fig. 8b and 8c. The contours accurately reveal the symmetric squeezing and stretching phenomena along the upper and lower edges of the cantilevered beam. When drilling rotations were not included, the iKS4 inverse element reconstructed a maximum horizontal displacement of 1.510 mm (absolute error of 7.64%). Upon including the drilling DOF, both the iKS4 and iQS4 inverse elements reconstructed a maximum horizontal displacement of 1.605 mm (absolute error of 1.83%).

The iFEM convergence chart presented in Fig. 9 illustrates the monotonic convergence of the reconstructed displacements for both configurations of the iKS4 inverse element (with and without drilling rotation DOF) and the iQS4 inverse element as the number of inverse elements increases. As anticipated, the iKS4 inverse shell element with drilling rotations demonstrates rapid convergence to the reference FEM solution, exhibiting behavior that is identical to that of the iQS4 inverse shell element. However, the straightforward inverse formulation of the iKS4 element is computationally more efficient, as its error functional

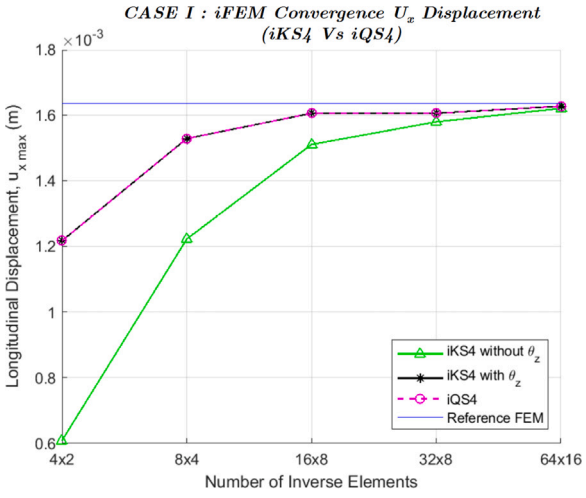

Fig. 9. Case I - Influence of inverse discretization on reconstructed horizontal displacement.

Table 1
Analysis details of Case - I.

Analysis	Sensors	Max $\mathbf{v}_y$	Max $\mathbf{u}_x$	Error [$\mathbf{v}_y$]
FEM	- - - - -	9.039 mm	1.635 mm	0.15% (abs)
iFEM-iKS4	16 × 8	8.890 mm	1.605 mm	1.49% (abs)
iFEM-iQS4	16 × 8	8.890 mm	1.605 mm	1.49% (abs)
Analytical Solution [31]		9.025 mm		

does not include shear components. This simplification reduces numerical complexity and incurs less computational overhead than more complex formulations that account for shear effects. The analysis details for Case-I are summarized in Table 1.

The analysis of the in-plane loading case highlights that the iKS4 element effectively reconstructs horizontal and vertical displacement profiles, achieving accuracy identical to that of the iQS4 inverse element. Both inverse shell elements incorporate drilling rotation DOF to improve element membrane behavior. However, distinctions in the reconstructed displacements between the iKS4 and iQS4 elements will

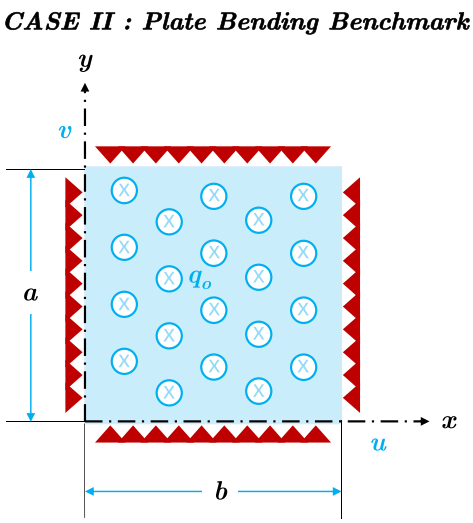

Fig. 10. Simply supported square plate under arbitrary uniform transverse load.

emerge in subsequent cases involving bending behavior, as these elements are based on different plate theory assumptions.

3.2. Out-of-plane loading (Case - II)

Numerical validation for the pure bending case is performed by reconsidering a classical textbook problem [31] to validate the proposed inverse formulation within the iFEM framework. An isotropic square plate with simply supported boundary conditions is subjected to a uniform transverse pressure q_o, as depicted in Fig. 10. The length a, width b, and thickness t of the plate are arbitrary, as the validation is based on dimensionless parameters, where $a = b = c$ and $t \ll c$, with c being the characteristic length of the plate.

For this case, a square plate $(a = b = 1)$ m is subjected to a uniform transverse pressure of $q_o = 10$ kN, and the thickness is set to $t = 0.01$ m, with material properties of $E = 200$ GPa and $\nu = 0.3$. Under given conditions, the maximum dimensionless transverse deflection [31] at the center of the plate is given as:

$$\bar{w}_{max} = w \times \frac{D}{q_o a^4} = -4.062 \times 10^{-3} \tag{36}$$

where $D = Et^3/12(1 - \nu^2)$ in the above dimensionless transverse displacement expression.

A high-fidelity FEM analysis is performed to simulate the analytical solution and corresponding deformation profiles (as shown in Fig. 11a). The normalized maximum out-of-plane displacement at the center of the simply supported plate is obtained as $\bar{w}_{max} = -4.062 \times 10^{-3}$, conforming well to the analytical solution outlined in Eq. (36). Since the deformations are purely due to bending, the strain distribution is anti-symmetric relative to the mid-plane. As the mid-plane undergoes no stretching, the surface strain values differ only in sign across the thickness. Consequently, strain measurements are needed only on either of the plate surfaces (e.g., $z = \pm t/2$). These discrete strain measures are subsequently used in the iFEM analysis to validate the iKS4 inverse element numerically.

The dimensionless transverse displacement reconstructed by the iKS4 inverse element using a 10 × 10 discretization scheme closely conforms to the analytical solution, showing an absolute error of only 0.12% in the maximum displacement (11b). The resulting displacement contour is virtually indistinguishable from the high-fidelity FEM analysis. Similarly, the iQS4 inverse element provides a reconstructed displacement field that agrees with the reference solution as shown in Fig. 11c. However, iQS4 converges slower when dealing with thin plate structures. To achieve comparable accuracy against the iKS4 inverse

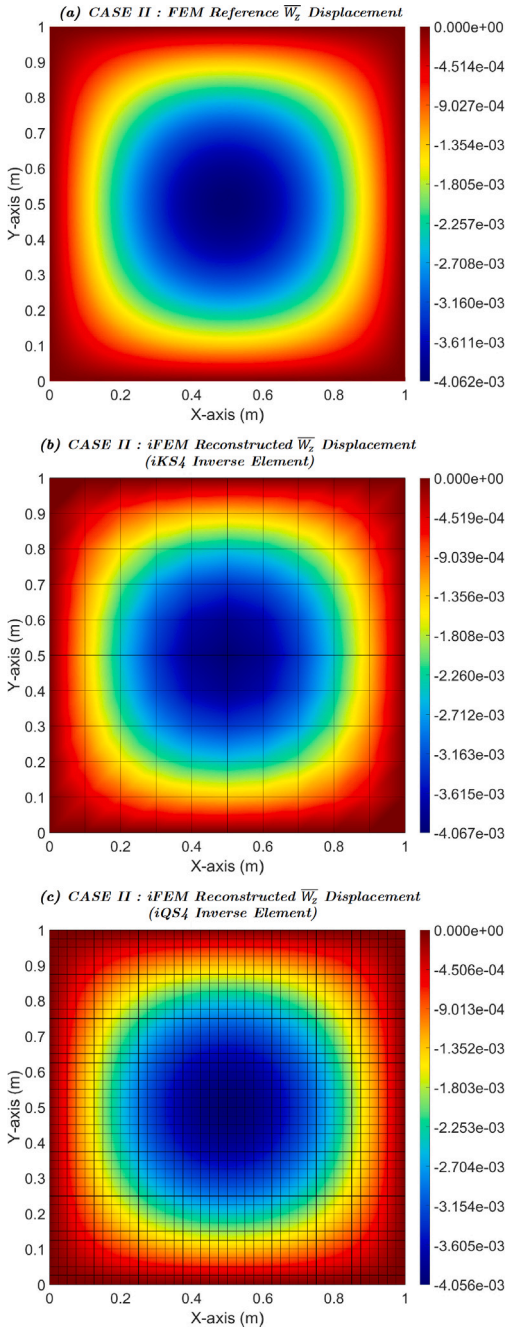

Fig. 11. Case II — Transverse displacement profiles: (a) FEM^{Ref}, (b) iFEM iKS4, and (c) iFEM iQS4.

element, iQS4 requires a finer 40 × 40 discretization. It yields an absolute error of 0.14% in predicting the maximum displacement at the center of the simply supported plate. Enhanced continuity of the discrete Kirchhoff shape functions in iKS4 inverse formulation allows for a coarser discretization while still accurately capturing the bending behavior of thin plates, with minimal impact on iFEM accuracy.

Fig. 12 illustrates the iFEM convergence trends for iKS4 and iQS4 inverse shell elements. It is evident from the chart that the iFEM solution approaches the analytical solution as the number of inverse elements increases. Notably, the iKS4 inverse element demonstrates faster convergence, requiring fewer inverse elements to reconstruct the bending response effectively. This efficiency is paramount for monitoring dynamic structural changes, enabling timely detection of potential

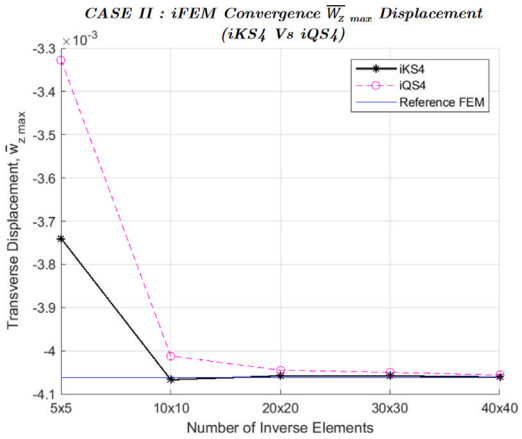

Fig. 12. Case II — Influence of inverse discretization on reconstructed transverse displacement.

Table 2
Analysis details of Case — II.

Analysis	Sensors	Max $\bar{w}_z$	Error [$\bar{w}_z$]
FEM	- - - - -	-4.062×10^{-3}	0.00% abs
iFEM-iKS4	10 × 10	-4.067×10^{-3}	0.12% abs
iFEM-iQS4	10 × 10	-4.012×10^{-3}	1.23% abs
Analytical Solution [31]	−4.062		

damage or anomalies while minimizing data processing time and computational costs. By requiring fewer onboard sensors, the iKS4 inverse element offers significant flexibility in sensor installation and substantially saves costs across various aspects of SHM applications. Therefore, for thin shell structures, using the iKS4 element improves the practicality and effectiveness of SHM systems in ensuring structural safety and reliability. Table 2 summarizes the key details of the iFEM analysis for this case.

3.3. General loading (Case - III)

General loading condition is now considered for a curved thin shell structure. The pinched cylinder with diaphragm boundary conditions is a well-known benchmark and is considered one of the most severe tests for both inextensional bending modes and complex membrane states. It is also part of the obstacle course for shell elements [32]. The cylinder, with a length $l = 600$, radius $r = 300$, and thickness $t = 3$, is subjected to a unit point load $P = 1$ at the center on opposite sides, as illustrated in Fig. 13. The cylinder has rigid end diaphragms; its material properties are $E = 3.0 \times 10^6$ and $\nu = 0.3$. Due to the problem's symmetry, only one octant of the cylinder is analyzed using FEM and iFEM analysis (as shown in Fig. 13). The discretized geometry is subjected to symmetric boundary conditions along the sides AB, BC, and CD, whereas it is subjected to rigid diaphragm boundary conditions along the AB end. A radial point load $-P/4$ is applied on the corner at point C. The reference solution for this case results in a maximum transverse displacement of $w_z = -1.824 \times 10^{-5}$ at the point of load application.

First, the high-fidelity FEM analysis is accomplished to replicate the reference result. The numerical solution gradually and consistently convergences to the reference value with the maximum radial displacement of -1.821×10^{-5}. The maximum displacement appears at a highly localized place (as depicted in Fig. 14a), precisely at the node where the radial point load is applied. This localized displacement is due to the concentrated nature of the load, which causes a significant deformation at the point of application. Synthetic strain data is generated based on the displacement profile obtained from the high-fidelity model for subsequent iFEM analysis. For three-dimensional structures, discrete strain measures are required on both surfaces for accurate reconstruction of

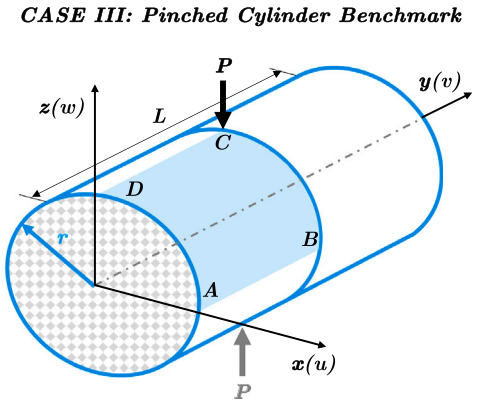

Fig. 13. Pinched cylinder with diaphragm boundary conditions.

Table 3
Analysis details of Case — III.

Analysis	Sensors	Max $\bar{w}_z$	Error [$\bar{w}_z$]
FEM	- - - - -	-1.821×10^{-5}	0.16% abs
iFEM-iKS4	24 × 24	-1.751×10^{-5}	4.00% abs
iFEM-iQS4	24 × 24	-1.694×10^{-5}	7.12% abs
Reference Solution [32]	-1.824×10^{-5}		

deformation profiles.

The comparison between the iKS4 and iQS4 inverse shell elements demonstrates a distinct advantage of the iKS4 in terms of both accuracy and sensor efficiency. The iKS4 element, using a 24 × 24 discretization, reconstructs a maximum radial deflection of -1.751×10^{-5} with an absolute error of 4.00%, despite the complexity of the problem (Fig. 14b). Conversely, the iQS4 element, even with a denser 32 × 32 discretization, reconstructs a slightly lower maximum radial displacement of -1.744×10^{-5} with a higher absolute error of 4.38% as depicted in Fig. 14(c). This comparison highlights that the iKS4 element provides more accurate displacement reconstruction with fewer inverse elements. Since the maximum displacement occurs in a highly localized region, finer discretization is required to reconstruct the displacement profile accurately. Interpolating discrete strain data (available at centroids) to other locations within the inverse elements can introduce slight interpolation errors in regions of steep displacement gradients. Consequently, a finer mesh is essential to capture these localized effects accurately. Table 3 summarizes the analysis details for Case III.

The influence of inverse discretization on the accuracy of displacement profile reconstruction is also studied for both iKS4 and iQS4 inverse shell elements (as shown in Fig. 15). With the increase in inverse elements, both iKS4 and iQS4 monotonically converge to the reference solution. The convergence trend lines clearly show that the iKS4 inverse element demonstrates rapid convergence compared to the iQS4 inverse element. This highlights the superior accuracy of the iKS4 element in displacement reconstruction, requiring fewer inverse elements while offering improved computational efficiency and cost savings. Hence, the proposed inverse shell formulation based on discrete Kirchhoff assumptions can be confidently used for thin shell structures in real-time SHM applications.

4. SHM applications of iKS4 inverse element

After successful numerical validation of the proposed inverse formulation, the iKS4 inverse shell element is now considered for real-world SHM applications, including shape sensing, defect identification, and structural damage assessment. In industrial SHM applications, determining the appropriate number of sensors for shape sensing is influenced by various factors, i.e., available space for onboard sensor installation, budget constraints, structural health, and computational

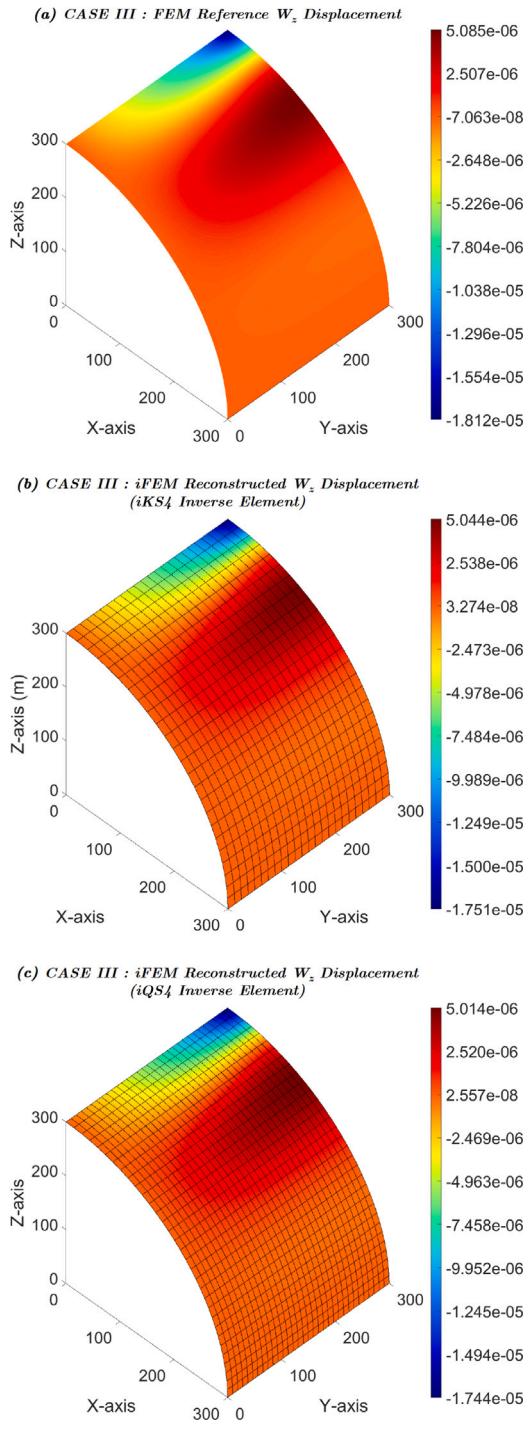

Fig. 14. Case III — Transverse displacement profiles: (a) FEM^{Ref}, (b) iFEM iKS4, and (c) iFEM iQS4.

accuracy and efficiency. Optimal sensor arrangement can be achieved by optimizing the iFEM framework for inverse element discretization, sensor locations within the spatial domain, and weighting functions in the error functional. More advanced techniques, such as sensor fusion and signal processing, enhance iFEM robustness under practicable sensor arrangement. Given that each structure experiences unique in-service loading conditions, no universal closed-form solution exists for determining optimal sensor arrangements across different structural systems.

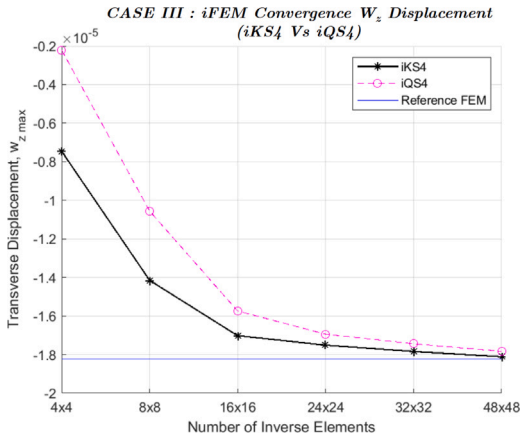

Fig. 15. Case III — Influence of inverse discretization on reconstructed transverse displacement.

In subsequent numerical cases, sparse sensor arrangements are defined using coarser discretizations and fewer sensors than dense sensor arrangements. The objective is to assess the robustness of the proposed iFEM algorithm using fewer sensors while maintaining consistency in variable factors influencing the error functional, i.e., sensor locations and weighting functions. Strain sensors are fixed at the centroid of the inverse elements for computing synthetic strain data. For sparse sensor arrangements, When discrete strain measures are available within an inverse element, the value of weighting coefficients is set to unity, i.e., $w_e = w_k = 1$. Conversely, when discrete strain measures are missing, these coefficients are set to minimal values, i.e., $w_e = w_k = 10^{-3}$. This approach minimizes variations by keeping these factors constant, allowing for a more straightforward interpretation of the iFEM results.

4.1. Shape-sensing of aircraft fuselage panel

Consider a wide-body aircraft operating at a cruise altitude of 39,000 ft while the cabin pressure is maintained at an equivalent altitude of 8000 ft. This configuration results in a pressure differential of 8.06 psi (approximately 0.56 bar). Under these conditions, the fuselage experiences a uniform pressure load of 55,571.71 Pa, accurately reflecting the operational in-service scenarios where cabin pressurization induces deformation within the fuselage structure.

The aircraft fuselage is constructed from thin, stiffened curved panels, which are securely screwed and sealed along their edges to the main airframe. This arrangement effectively simulates a clamped boundary condition (BC) on all sides, enhancing the structural integrity required to withstand aerodynamic loads and internal pressures during flight.

The geometry of the fuselage panel, illustrated in Fig. 16, includes a radius of $r = 1.960$ m and a thickness of $t = 0.002$ m, with dimensions $a = 0.563$ m, $b = 0.795$ m, $c = 0.198$ m, and $d = 0.281$ m. Reinforcing the panel are three stiffeners, each with a height of $l = 0.019$ m, positioned along the width of the panel, in addition to a main stiffener located at the center, extending along its length, with a height of $p = 0.038$ m. The panel is fabricated from Aluminum Alloy 2024-T3, a material commonly employed in aerospace applications due to its favorable strength-to-weight ratio. The material properties are characterized by Young's modulus of $E = 73.1$ GPa and a Poisson's ratio of $\nu = 0.33$.

In this case, the fuselage stiffened panel is initially analyzed via a high-fidelity FEM model using 4160 structured quadrilateral elements. Under the specified cabin pressurization conditions, the stiffened panel experiences significant transverse deformations, often called "bulging," which usually occurs between the frames and stringers. This deformation results in a wavy surface profile influencing aerodynamic efficiency. Fig. 17a illustrates the stiffened panel's transverse displacement

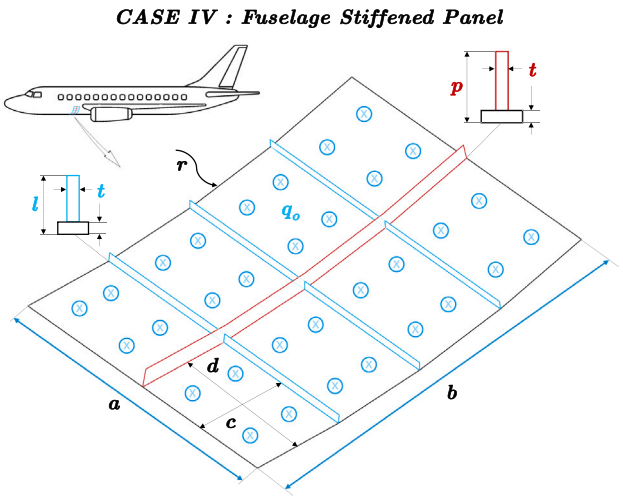

Fig. 16. Case IV — Aircraft fuselage stiffened panel under cabin pressurization.

profile, highlighting a maximum transverse displacement of 1.668 mm at the center of the stiffened panel. The displacement field obtained through the high-fidelity FEM model generates synthetic strain data and serves as the reference solution for iFEM analysis.

For subsequent shape-sensing analysis, the iFEM framework utilizes a considerably coarse discretization scheme with 260 iKS4 inverse shell elements mapping the entire geometric domain (illustrated in Fig. 17b). Only 62 inverse elements with discrete strain measures are provided to reconstruct the displacement field considering a practicable sensor arrangement scenario. The inverse elements with discrete strain measures are highlighted in yellow (refer Fig. 17b), and sensor locations are indicated in red dots at the centroids of inverse elements.

The reconstructed transverse displacement contour shows good agreement with the reference displacement contour obtained from the reference FEM solution as depicted in Fig. 17c. Notably, the maximum reconstructed transverse displacement exhibits an absolute error of only 2.4%, displaying the effectiveness of the iKS4 inverse shell element in capturing the deformation characteristics of the fuselage under cabin pressurization conditions. It offers significant advantages over FSDT-based inverse elements in addressing the challenges of thin aerospace structures, providing enhanced reliability and computational efficiency for shape-sensing applications. The proposed inverse formulation requires fewer onboard strain sensors while accurately reconstructing full-field displacement profiles. While the sparse sensor arrangement explored in this study has proven effective for this scenario, it aims to inspire further designs for applications involving more complex structures.

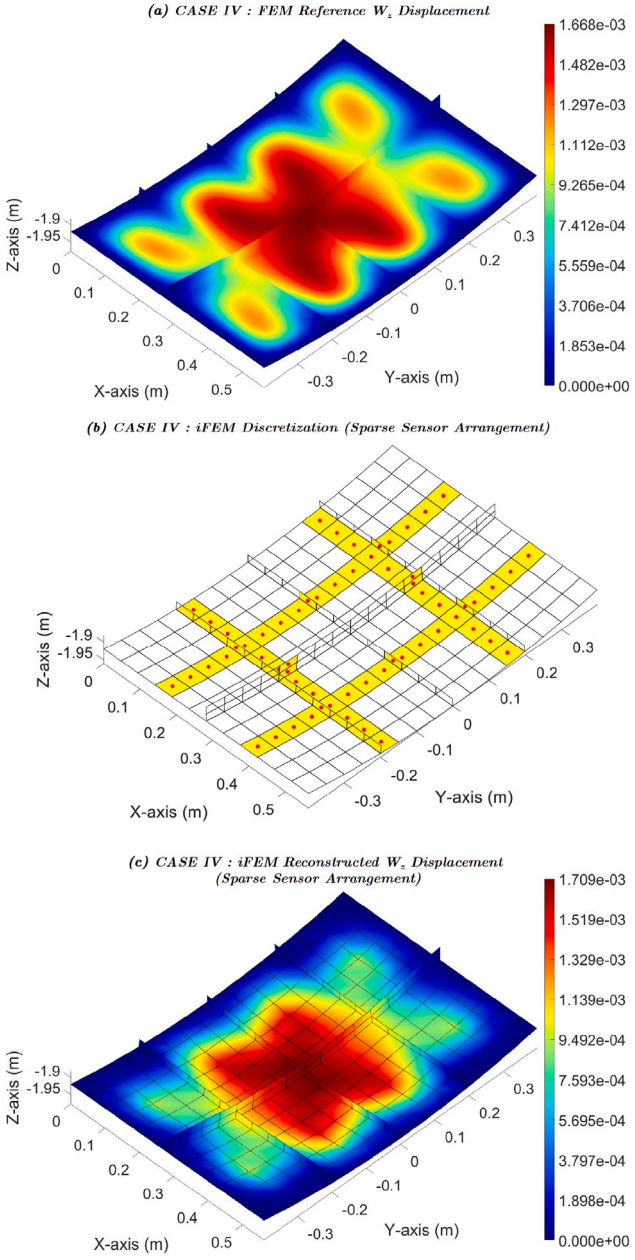

Fig. 17. Case IV — Transverse displacement profile: (a) FEM^{Ref}, (b) Sparse sensor arrangement, and (c) iFEM iKS4 under sparse sensor arrangement.

4.2. Detecting material discontinuities

In aerospace applications, the potential for Foreign Object Damage (FOD), bird strikes on aircraft, and impacts from space debris on spacecraft often result in material discontinuities necessitating real-time detection as part of SHM implementation. Accurate assessment of these discontinuities is crucial for effective decision-making regarding mission continuation or termination, ensuring the safety and reliability of aerospace operations.

The presence of material discontinuities can be effectively simulated using a plate under tensile loading with a geometric discontinuity in the form of a hole at the center of the plate. The stress concentration effects around the hole can be successfully reconstructed using iFEM analysis. For the given scenario, consider a plate of length $a = 0.1$ m, width $b = 0.3$ m, and thickness $t = 0.001$ m subjected to tensile loading $P = 1.2\times10^6$ N/m along the horizontal direction as illustrated in Fig. 18.

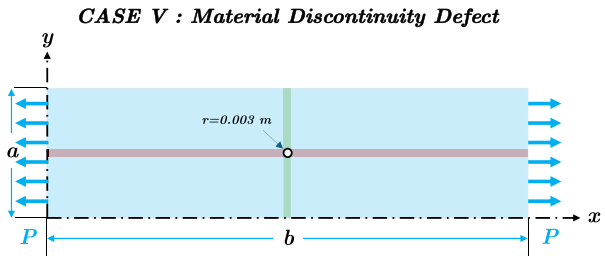

Fig. 18. Case V — Material discontinuity defect under tensile loading.

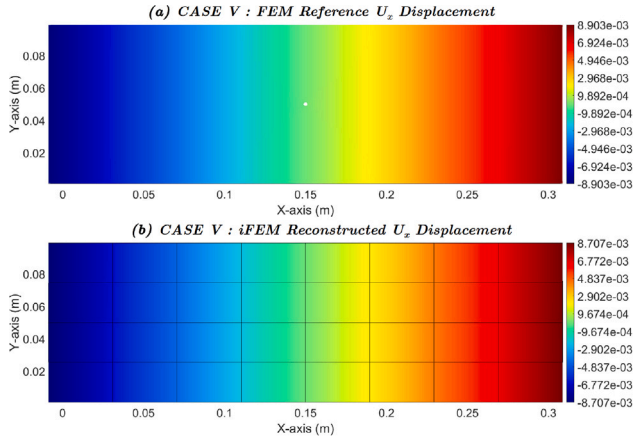

Fig. 19. Case V — Horizontal displacement profiles: (a) FEM^{Ref} and (b) iFEM iKS4.

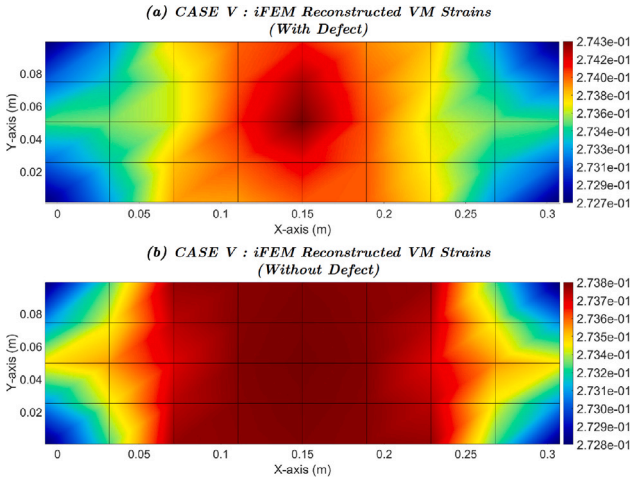

Fig. 20. Case V — iFEM iKS4 reconstructed equivalent von Mises strains: (a) With material discontinuity and (b) Without material discontinuity.

The material discontinuity in the form of a punched hole is modeled at the center of the plate having a radius $r = 0.003$ m. Symmetric boundary conditions restricting horizontal and vertical translations are applied along green and red lines. Isotropic material properties considered for the plates are $E = 200$ GPa and $\nu = 0.3$.

The high-fidelity FEM analysis is conducted in the presence of a geometric discontinuity, and discrete strain data is generated based on the reference displacement field (shown in Fig. 19a). Subsequently, the iFEM analysis employs 32 structured inverse quadrilateral elements to reconstruct the horizontal displacement field, as illustrated in Fig. 19b. The reference and reconstructed displacement contours are virtually indistinguishable; moreover, the smaller size of the material discontinuity (modeled as a hole) does not introduce significant variations in the reference and reconstructed displacement fields. To overcome the challenge of detecting minor defects from the reconstructed displacement field, equivalent von Mises strains can be plotted to identify and quantify subtle discontinuities. These equivalent von Mises strains can be computed using the following mathematical expression:

$$\varepsilon_{vm} = \sqrt{(\varepsilon_1)^2 - \varepsilon_1\varepsilon_2 + (\varepsilon_2)^2} \tag{37}$$

where, ε_1 and ε_2 can be calculated as:

$$\begin{cases} \varepsilon_1 &= \frac{\varepsilon_{xx}+\varepsilon_{yy}}{2} + \sqrt{\left(\frac{\varepsilon_{xx}-\varepsilon_{yy}}{2}\right)^2 + \left(\frac{\gamma_{xy}}{2}\right)^2} \\ \varepsilon_2 &= \frac{\varepsilon_{xx}+\varepsilon_{yy}}{2} - \sqrt{\left(\frac{\varepsilon_{xx}-\varepsilon_{yy}}{2}\right)^2 + \left(\frac{\gamma_{xy}}{2}\right)^2} \end{cases}$$

Here, ε_{xx}, ε_{yy}, and γ_{xy} are the in-plane normal and shear strain components. These von Mises strain contours facilitate the identification of localized defects by highlighting abnormal strain distributions within the structure.

The reconstructed displacement field is used to compute the von Mises strain field. Fig. 20 presents two von Mises strain contours: one for the plate with a material discontinuity defect and the other for the defect-free plate. The region of high von Mises strain gradient in Fig. 20a accurately identifies the location of the punched hole in the defective plate. In contrast, Fig. 20b illustrates the von Mises strain contour for the plate without the defect, allowing for a direct comparison between the two cases. This comparison highlights the distinct differences in strain distribution due to the geometric discontinuity. The equivalent von Mises strain contour demonstrates the iKS4 inverse element's ability to detect material discontinuities, highlighting its potential for aerospace SHM applications. It is particularly effective for identifying and resolving minor geometric defects in thin structures.

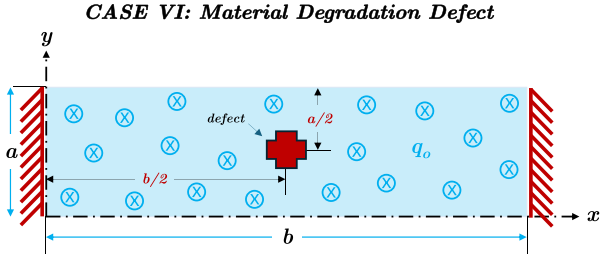

Fig. 21. Case VI — Material degradation defect under transverse loading.

4.3. Detecting material degradation

In practical engineering applications, not all structural defects appear as geometric discontinuities, as discussed in the previous case. Material degradation from cyclic loading is a significant concern in aerospace structures, as repeated stress can cause fatigue and gradual deterioration of material properties. Material degradation effects are often latent, not readily appearing as visible structural defects or material discontinuities. The hidden nature of these damages complicates early detection, posing risks to the integrity and safety of critical airframe components. Therefore, an effective SHM system enables early detection of material degradation and facilitates timely maintenance, thereby ensuring the reliability and safety of aerospace structures.

In this analysis, the geometric dimensions and material properties of the structural specimen considered in the previous Section 4.2 remain unchanged. However, the plate's left and right edges are fixed, and a uniform transverse pressure of $q_o = 1000$ Pa is applied. The material discontinuity is now replaced with a material degradation defect, as illustrated in Fig. 21. To effectively model this defected material domain in FEM analysis, a damage degradation factor, λ, is introduced, where $0 < \lambda < 1$. $\lambda = 1$ represents a healthy structural state that retains its material properties, while $0 < \lambda < 1$ corresponds to the degraded state of the material. In high-fidelity forward FEM analysis, the material degradation factor is set to $\lambda = 0.6$ and is incorporated into the element stiffness formulation to represent the degraded stiffness matrix accurately. The displacement field obtained from the reference FEM analysis is then used to generate discrete strain measures for the subsequent iFEM analysis. For brevity, reconstructed displacement profiles are discussed here to access the defect resolution capability of the iKS4 inverse shell element.

The iFEM results for the reconstructed transverse deflection w_z and bending rotations θ_x and θ_y are presented in Fig. 22a, 22b, and

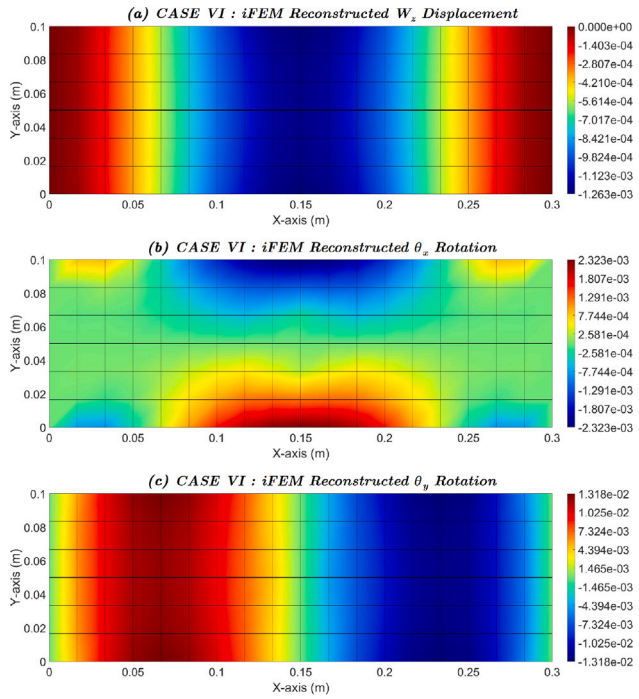

Fig. 22. Case VI — iFEM iKS4 reconstructed displacement profiles: (a) Transverse displacement, (b) Bending rotation θ_x, and (c) Bending rotation θ_y.

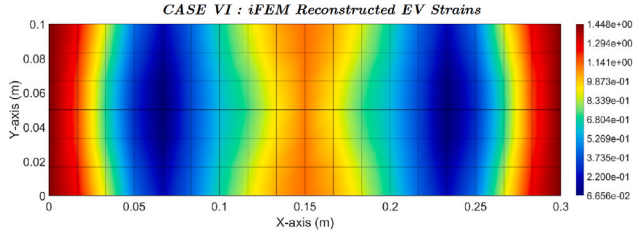

Fig. 23. Case VI — iFEM iKS4 reconstructed equivalent von Mises strains.

22c, respectively. While the w_z and θ_y displacement contours exhibit a slight bias in the regions affected by the material degradation defect, the bending rotation contour for θ_x illustrates a more pronounced displacement variation within the defective domain of the plate. The sensitivity of the reconstructed transverse displacement w_z and bending rotations θ_x and θ_y to the material degradation defect depends on the defect's placement and orientation, as well as the given boundary and loading conditions.

In the previous case, the von Mises strain contour exhibited reliable sensitivity for detecting material discontinuities that can be physically measured, facilitating practical structural health assessments based on defect sizing following OEM guidelines. However, in the case of material degradation defects, the von Mises strain contour (as shown in Fig. 23) is insufficient for effective defect detection and structural health assessment during field and intermediate-level maintenance operations. Therefore, in such scenarios, employing damage index criteria based on von Mises strains offers more accurate insights into defect location, sizing, and a comprehensive structural integrity evaluation. The damage index criterion is more general and allows for structural health assessment in the presence of various defects, including material degradation, material discontinuities (cracks, voids), delaminations, and corrosion. Mathematically, the damage index can be computed as:

$$\mathrm{DI}\left(\varepsilon_{vm}\right) = \left|\frac{\varepsilon_{vm} - \varepsilon^{*}_{vm}}{\varepsilon^{max}_{vm}}\right| \times 100\% \tag{38}$$

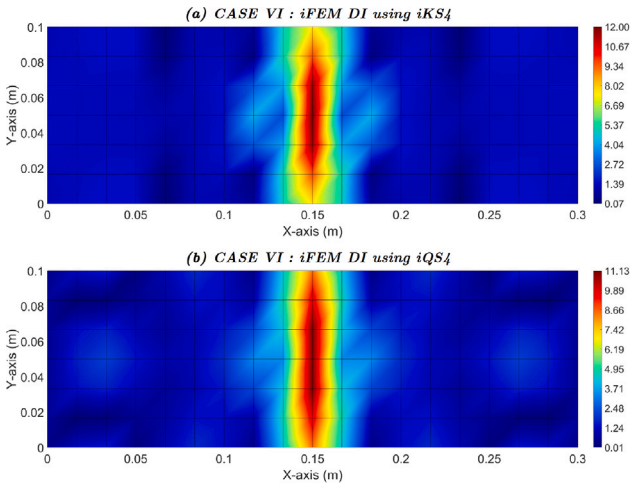

Fig. 24. Case VI — iFEM reconstructed damage index profile: (a) iKS4 inverse shell element and (b) iQS4 inverse shell element.

where ε_{vm} represents the equivalent von Mises strain calculated using the iFEM framework under the assumption of intact material and ε^{max}_{vm} denotes the maximum reconstructed von Mises strain observed during the analysis. The term ε^{*}_{vm} represents the reconstructed von Mises strains for structures exhibiting material degradation defects. In SHM applications, the damage index (DI) is a valuable metric that quantifies the severity of material degradation and enables informed decision-making regarding preventive maintenance to ensure structural safety and reliability.

Fig. 24 presents the damage index (DI) contours for the given case, providing a comparative analysis of the iKS4 and iQS4 inverse shell elements. The damage index values assist in interpreting structural integrity, with a DI $\approx$ 10 typically classified as minor damage. While such damage may not significantly compromise structural integrity, it does warrant ongoing monitoring.

Fig. 24a shows that the iKS4 inverse element performs better in structural damage assessment by providing precise damage localization, higher DI sensitivity, and smoother gradient transitions. The contour plot illustrates a peak DI of 12.00 at the center of the structure, accurately identifying and outlining a well-defined damage zone. In contrast, the iQS4 inverse element produces a broader and less precise damage zone, with a peak DI value of 11.13, as depicted in Fig. 24b. The broader damage zone may result in overestimating the affected area while underestimating the damage severity, leading to inefficient and less reliable structural health evaluation. This analysis highlights the utility of the iKS4 inverse shell element in assessing structural health and identifying areas requiring preventive maintenance, contributing to the overall reliability and safety of aerospace structures.

5. Conclusion

This study uses discrete Kirchhoff assumptions to introduce a four-node quadrilateral inverse shell element (iKS4) for thin plates and shell structures commonly used in aerospace. The inverse formulation neglects transverse shear effects, consistent with discrete Kirchhoff assumptions, simplifies the error functional, and enhances computational efficiency compared to existing inverse elements based on First-Order Shear Deformation Theory (FSDT). Incorporating the drilling degree of freedom (DOF) improves interelement continuity and improves compatibility between the membrane and bending behavior.

The proposed inverse formulation is numerically validated against established benchmark problems under in-plane, bending, and mixed-loading conditions. Its full-field displacement reconstruction capability is compared to the existing iQS4 inverse shell element. The proposed formulation exhibits numerical stability and outperforms the

iQS4 inverse shell element in convergence rates for pure bending and general loading conditions. Consequently, the iKS4 inverse element offers computational advantage and improved accuracy while reducing the number of onboard sensors needed in real-time shape-sensing applications.

After extensive numerical validation, the iKS4 inverse shell element is further evaluated for Structural Health Monitoring (SHM) applications, considering real-world cases from the aerospace industry. The inverse formulation shows reliable accuracy in shape-sensing and defect resolution studies, successfully detecting and quantifying material discontinuities and degradation defects. These capabilities are critical for modern health monitoring systems, facilitating efficient maintenance scheduling while ensuring airframe reliability and safety. Eventually, the iKS4 inverse shell element, with its straightforward inverse formulation and computational efficiency, holds significant potential for aerospace Structural Health Monitoring (SHM) applications by reducing sensor requirements and minimizing overall project costs.

CRediT authorship contribution statement

Ihtisham Khalid: Writing – review & editing, Writing – original draft, Validation, Methodology, Formal analysis, Conceptualization. **Zahid Ahmed Qureshi:** Writing – review & editing, Software, Methodology, Conceptualization. **Selda Oterkus:** Writing – review & editing, Supervision, Resources, Methodology, Conceptualization. **Erkan Oterkus:** Writing – review & editing, Validation, Supervision, Methodology, Investigation.

Declaration of competing interest

The authors declare that they have no known competing financial interests or personal relationships that could have appeared to influence the work reported in this paper.

Appendix

A.1. Quadrilateral basis functions

The explicit forms of isoparametric bi-linear basis functions used for the quadrilateral inverse element are expressed here. These basis functions are utilized for geometric mapping and interpolation of the in-plane translational displacement variables.

$$N_1 = -\frac{(\eta-1)(\xi-1)}{4} \tag{A.1.1a}$$

$$N_2 = -\frac{(\eta-1)(\xi+1)}{4} \tag{A.1.1b}$$

$$N_3 = \frac{(\eta+1)(\xi+1)}{4} \tag{A.1.1c}$$

$$N_4 = -\frac{(\eta+1)(\xi-1)}{4} \tag{A.1.1d}$$

where ξ and η are the natural coordinates of the four-node quadrilateral element.

Similarly, the explicit forms of quadratic basis functions for the eight-node quadrilateral element are outlined below for interpolating out-of-plane displacement variables.

$$S_1 = -\frac{1}{4}(1-\xi)(1-\eta)(1+\xi+\eta) \tag{A.1.2a}$$

$$S_2 = -\frac{1}{4}(1+\xi)(1-\eta)(1-\xi+\eta) \tag{A.1.2b}$$

$$S_3 = -\frac{1}{4}(1+\xi)(1+\eta)(1-\xi-\eta) \tag{A.1.2c}$$

$$S_4 = -\frac{1}{4}(1-\xi)(1+\eta)(1+\xi-\eta) \tag{A.1.2d}$$

$$S_5 = \frac{1}{2}(1-\xi^2)(1-\eta) \tag{A.1.2e}$$

$$S_6 = \frac{1}{2}(1+\xi)(1-\eta^2) \tag{A.1.2f}$$

$$S_7 = \frac{1}{2}(1-\xi^2)(1+\eta) \tag{A.1.2g}$$

$$S_8 = \frac{1}{2}(1-\xi)(1-\eta^2) \tag{A.1.2h}$$

Here, ξ and η are the natural coordinates of the eight-node quadrilateral element.

A.2. Drilling rotation DOF

The anisoparametric shape functions L_i and M_i are crucial for capturing rotational degrees of freedom in finite element models. These functions allow accurate representation of drilling rotations and are defined as follows for the inverse quadrilateral element:

$$L_1 = \frac{S_8 y_{14} - S_5 y_{21}}{8} \tag{A.2.1a}$$

$$L_2 = \frac{S_5 y_{21} - S_6 y_{32}}{8} \tag{A.2.1b}$$

$$L_3 = \frac{S_6 y_{32} - S_7 y_{43}}{8} \tag{A.2.1c}$$

$$L_4 = \frac{S_7 y_{43} - S_8 y_{14}}{8} \tag{A.2.1d}$$

$$M_1 = \frac{-S_8 x_{14} + S_5 x_{21}}{8} \tag{A.2.2a}$$

$$M_2 = \frac{-S_5 x_{21} + S_6 x_{32}}{8} \tag{A.2.2b}$$

$$M_3 = \frac{-S_6 x_{32} + S_7 x_{43}}{8} \tag{A.2.2c}$$

$$M_4 = \frac{-S_7 x_{43} + S_8 x_{14}}{8} \tag{A.2.2d}$$

Here, S_5 to S_8 are basis functions for the eight-node quadrilateral element defined in Eqs. (A.1.2e)–(A.1.2h), and the nodal distances x_{ij} and y_{ij} defined as:

$$x_{14} = x_1 - x_4, \quad y_{14} = y_1 - y_4$$
$$x_{21} = x_2 - x_1, \quad y_{21} = y_2 - y_1$$
$$x_{32} = x_3 - x_2, \quad y_{32} = y_3 - y_2$$
$$x_{43} = x_4 - x_3, \quad y_{43} = y_4 - y_3$$

A.3. Discrete Kirchhoff's quadrilateral shape functions

In this section, the shape function vectors $\boldsymbol{H}^x$ and $\boldsymbol{H}^y$ are defined in the local element coordinate system based on discrete Kirchhoff assumptions and proposed by Batoz et al. [26]. The anisoparametric shape functions satisfy continuity requirements for displacement and rotation across the element edges, which is crucial for accurate structural analysis, particularly for thin plates.

$$\boldsymbol{H}^x = \begin{bmatrix} \frac{3}{2}\left(a_5 S_5 - a_8 S_8\right) \\ b_5 S_5 + b_8 S_8 \\ S_1 - c_5 S_5 - c_8 S_8 \\ \frac{3}{2}\left(a_6 S_6 - a_5 S_5\right) \\ b_6 S_6 + b_5 S_5 \\ S_2 - c_6 S_6 - c_5 S_5 \\ \frac{3}{2}\left(a_7 S_7 - a_6 S_6\right) \\ b_7 S_7 + b_6 S_6 \\ S_3 - c_7 S_7 - c_6 S_6 \\ \frac{3}{2}\left(a_8 S_8 - a_7 S_7\right) \\ b_8 S_8 + b_7 S_7 \\ S_4 - c_8 S_8 - c_7 S_7 \end{bmatrix} \tag{A.3.1}$$

$$\boldsymbol{H}^{y}=\begin{bmatrix}\frac{3}{2}\left(d_5S_5-d_8S_8\right)\\ -S_1+e_5S_5+e_8S_8\\ -b_5S_5-b_8S_8\\ \frac{3}{2}\left(d_6S_6-d_5S_5\right)\\ -S_2+e_6S_6+e_5S_5\\ -b_6S_6-b_5S_5\\ \frac{3}{2}\left(d_7S_7-d_6S_6\right)\\ -S_3+e_7S_7+e_6S_6\\ -b_7S_7-b_6S_6\\ \frac{3}{2}\left(d_8S_8-d_7S_7\right)\\ -S_4+e_8S_8+e_7S_7\\ -b_8S_8-b_7S_7\end{bmatrix} \tag{A.3.2}$$

Here, S_5 to S_8 are basis functions for the eight-node quadrilateral element defined in Eqs. (A.1.2e)–(A.1.2h). Since the shape functions are derived based on the local coordinates of the quadrilateral element, denoted by subscripts p and q, representing the positions of the element nodes. The expressions for x_{pq}, y_{pq}, and r_{pq} define the geometric relationships between adjacent nodes, essential for ensuring the consistency and smoothness of the shape functions.

$$x_{pq}=x_p-x_q \tag{A.3.3}$$

$$y_{pq}=y_p-y_q \tag{A.3.4}$$

$$r_{pq}=x_{pq}^2+y_{pq}^2 \tag{A.3.5}$$

$$where r=5,6,7,8 \quad when pq=12,23,34,41$$

The coefficients a_r, b_r, c_r, d_r, and e_r depend on the quadrilateral's geometry and node positions.

$$a_r=-\frac{x_{pq}}{r_{pq}} \tag{A.3.6}$$

$$b_r=\frac{3}{4}\frac{x_{pq}y_{pq}}{r_{pq}} \tag{A.3.7}$$

$$c_r=\frac{\frac{1}{4}x_{pq}^2-\frac{1}{2}y_{pq}^2}{r_{pq}} \tag{A.3.8}$$

$$d_r=-\frac{y_{pq}}{r_{pq}} \tag{A.3.9}$$

$$e_r=\frac{\frac{1}{4}y_{pq}^2-\frac{1}{2}x_{pq}^2}{r_{pq}} \tag{A.3.10}$$

A.4. Coordinate transformation system

Typically, two-dimensional shell elements, formulated by superimposing membrane and bending components, are computationally efficient and relatively simple. In such formulations, the transformation between the element's local and global coordinate systems is crucial, particularly for the proposed inverse shell element. Given the position vectors between any two nodes within the element, the unit vectors defining the local coordinate system (x', y', z') can be determined using vector calculus.

The vector between two nodes i and j is defined as:

$$\mathbf{V}_{ij}^{e}=\begin{Bmatrix}x_j-x_i\\ y_j-y_i\\ z_j-z_i\end{Bmatrix}^{e}=\begin{Bmatrix}x_{ij}\\ y_{ij}\\ z_{ij}\end{Bmatrix}^{e} \tag{A.3.11}$$

The corresponding unit vector is:

$$\hat{\mathbf{v}}_{ij}^{e}=\frac{1}{l_{ij}^{e}}\begin{Bmatrix}x_{ij}\\ y_{ij}\\ z_{ij}\end{Bmatrix}^{e}=\frac{\mathbf{V}_{ij}^{e}}{\|\mathbf{V}_{ij}^{e}\|} \tag{A.3.12}$$

where l_{ij}^{e} is the length of the side between nodes i and j.

$$l_{ij}^{e}=\sqrt{\left(x_{ij}^2+y_{ij}^2+z_{ij}^2\right)^{e}} \tag{A.3.13}$$

First, the unit vector along the local z' axis is determined to define the local coordinate system. For the given quadrilateral inverse element, this transverse local unit vector is calculated using the cross product of vectors $\mathbf{V}_{12}^{e}$ and $\mathbf{V}_{13}^{e}$, which lie along nodes 1–2 and 1–3, respectively.

$$\hat{\mathbf{v}}_{z'}^{e}=\frac{\mathbf{V}_{12}^{e}\times\mathbf{V}_{13}^{e}}{\|\mathbf{V}_{12}^{e}\times\mathbf{V}_{13}^{e}\|}=\begin{Bmatrix}\lambda_{z'x}\\ \lambda_{z'y}\\ \lambda_{z'z}\end{Bmatrix}^{e} \tag{A.3.14}$$

The local y' axis is now defined by intersecting the element with a plane parallel to the global yz plane, and the unit vector along the local y' axis is:

$$\hat{\mathbf{v}}_{y'}^{e}=\begin{Bmatrix}0\\ \lambda_{y'y}\\ \lambda_{y'z}\end{Bmatrix}^{e} \tag{A.3.15}$$

Here, the projection of x' onto the global y axis is zero. The unknown components $\lambda_{y'y}$ and $\lambda_{y'z}$ are determined by ensuring the unit vector $\hat{\mathbf{v}}_{y'}^{e}$ maintains a length of unity:

$$\left(\lambda_{y'y}^{e}\right)^2+\left(\lambda_{y'z}^{e}\right)^2=1 \tag{A.3.16}$$

and the second necessary equation comes from the condition that the scalar product of the unit vectors $\mathbf{v}_{y'}^{e}$ and $\mathbf{v}_{z'}^{e}$ is zero. Additionally, the unit vectors $\hat{\mathbf{v}}_{y'}^{e}$ and $\hat{\mathbf{v}}_{z'}^{e}$ must be orthogonal, which provides the second equation:

$$\lambda_{y'y}^{e}\lambda_{z'y}^{e}+\lambda_{y'z}^{e}\lambda_{z'z}^{e}=0 \tag{A.3.17}$$

From Eq. (A.3.16) and (A.3.17), the unknown components $(\lambda_{y'y}, \lambda_{y'z})$ of the unit vector $\hat{\mathbf{v}}_{y'}^{e}$ can be obtained easily.

$$\lambda_{y'y}^{e}=\frac{1}{\sqrt{1+\left(\frac{\lambda_{z'z}}{\lambda_{z'y}^{e}}\right)^2}} \tag{A.3.18}$$

$$\lambda_{y'z}^{e}=\frac{1}{\sqrt{1+\left(\frac{\lambda_{z'y}^{e}}{\lambda_{z'z}^{e}}\right)^2}} \tag{A.3.19}$$

Finally, the unit vector along the local x' axis is obtained by taking the cross product of $\hat{\mathbf{v}}_{y'}^{e}$ and $\hat{\mathbf{v}}_{z'}^{e}$.

$$\hat{\mathbf{v}}_{x'}^{e}=\hat{\mathbf{v}}_{y'}^{e}\times\hat{\mathbf{v}}_{z'}^{e}=\begin{Bmatrix}\lambda_{x'x}\\ \lambda_{x'y}\\ \lambda_{x'z}\end{Bmatrix}^{e} \tag{A.3.20}$$

These local unit vectors $\hat{\mathbf{v}}_{x'}^{e}, \hat{\mathbf{v}}_{y'}^{e}, \hat{\mathbf{v}}_{z'}^{e}$ define the direction cosines that describe the orientation of the local coordinate system $[x', y', z']$ relative to the global coordinate system $[x, y, z]$. The transformation matrix $\boldsymbol{T}$ can be assembled using Eq. (A.3.14), (A.3.15) and (A.3.20).

$$\boldsymbol{T}=\begin{pmatrix}\lambda_{x'x}^{e} & \lambda_{x'y}^{e} & \lambda_{x'z}^{e}\\ \lambda_{y'x}^{e} & \lambda_{y'y}^{e} & \lambda_{y'z}^{e}\\ \lambda_{z'x}^{e} & \lambda_{z'y}^{e} & \lambda_{z'z}^{e}\end{pmatrix} \tag{A.3.21}$$

Here, $\boldsymbol{T}$ is a 3×3 matrix that transforms global coordinates $[x, y, z]$ to local coordinates $[x', y', z'] = \boldsymbol{T}[x, y, z]$. This transformation is critical in shell element formulations to ensure accurate alignment between local and global coordinate systems.

After computing the local stiffness matrix k'^{e}, it is transformed into a global stiffness $\boldsymbol{k}^{e}$ matrix using the element transformation matrix $\boldsymbol{T}^{e}$.

$$\boldsymbol{k}^{e}=\left[\boldsymbol{T}^{e}\right]^{\mathrm{T}}\boldsymbol{k}'^{e}\left[\boldsymbol{T}^{e}\right] \tag{A.3.22}$$

For the entire iKS4 inverse shell element, which has six degrees of freedom (DOFs) per node, the complete element transformation matrix

is represented as:

$$\boldsymbol{T}^e = \begin{bmatrix} \boldsymbol{T} & & & & & \\ & \boldsymbol{T} & & & \boldsymbol{0} & \\ & & \boldsymbol{T} & & & \\ & & & \boldsymbol{T} & & \\ & sym & & & \boldsymbol{T} & \\ & & & & & \boldsymbol{T} \end{bmatrix} \tag{A.3.23}$$

This 24×24 block-diagonal matrix $\boldsymbol{T}^e$ is used to transform local element stiffness matrices into the global coordinate system. Its structure is essential for accurately mapping the local stiffness contributions to the global system, especially in three-dimensional problems where each node has six DOFs (three translations and three rotations).

Data availability

Data will be made available on request.

References

[1] S. Hassani, U. Dackermann, A systematic review of advanced sensor technologies for non-destructive testing and structural health monitoring, Sensors 23 (4) (2023) 2204.

[2] W.L. Ko, W.L. Richards, V.T. Tran, Displacement Theories for In-Flight Deformed Shape Predictions of Aerospace Structures, Technical Report, NASA, 2007.

[3] W.L. Ko, W.L. Richards, V.T. Fleischer, Applications of ko displacement theory to the deformed shape predictions of the doubly-tapered ikhana wing, Technical Report, NASA, 2009.

[4] G. Foss, E. Haugse, Using modal test results to develop strain to displacement transformations, in: Proceedings of the 13th International Modal Analysis Conference, vol. 2460, 1995, p. 112.

[5] M. Gopinathan, G.A. Pajunen, P. Neelakanta, M. Arockaisamy, Recursive estimation of displacement and velocity in a cantilever beam using a measured set of distributed strain data, J. Intell. Mater. Syst. Struct. 6 (4) (1995) 537–549.

[6] A.C. Pisoni, C. Santolini, D.E. Hauf, S. Dubowsky, Displacements in a vibrating body by strain gage measurements, in: Proceedings-SPIE the International Society for Optical Engineering, Citeseer, 1995, 119–119.

[7] S. Shkarayev, R. Krashantisa, A. Tessler, An inverse interpolation method utilizing in-flight strain measurements for determining loads and structural response of aerospace vehicles, 2004.

[8] J.S. Alexander Tessler, A variational principle for reconstruction of elastic deformations in shear deformable plates and shells, NASA (2003).

[9] H. Guo, X. Zhuang, T. Rabczuk, A deep collocation method for the bending analysis of Kirchhoff plate, 2021, arXiv preprint arXiv:2102.02617.

[10] H. Hu, L. Qi, X. Chao, Physics-informed neural networks (PINN) for computational solid mechanics: Numerical frameworks and applications, Thin-Walled Struct. (2024) 112495.

[11] X. Zhuang, H. Guo, N. Alajlan, H. Zhu, T. Rabczuk, Deep autoencoder based energy method for the bending, vibration, and buckling analysis of Kirchhoff plates with transfer learning, Eur. J. Mech. A Solids 87 (2021) 104225.

[12] A. Tessler, J.L. Spangler, Inverse FEM for full-field reconstruction of elastic deformations in shear deformable plates and shells, in: 2nd European Workshop on Structural Health Monitoring, 2004.

[13] A. Kefal, E. Oterkus, A. Tessler, J.L. Spangler, A quadrilateral inverse-shell element with drilling degrees of freedom for shape sensing and structural health monitoring, Eng. Sci. Technol., Int. J. 19 (3) (2016) 1299–1313.

[14] A. Kefal, An efficient curved inverse-shell element for shape sensing and structural health monitoring of cylindrical marine structures, Ocean Eng. 188 (2019) 106262.

[15] I. Khalid, Z.A. Qureshi, H.A. Khan, S. Oterkus, E. Oterkus, A quadrilateral inverse plate element for real-time shape-sensing and structural health monitoring of thin plate structures, Comput. Struct. 305 (2024) 107551.

[16] A. Kefal, E. Oterkus, Isogeometric iFEM analysis of thin shell structures, Sensors 20 (9) (2020) 2685.

[17] Y. Dirik, S. Oterkus, E. Oterkus, Isogeometric mindlin-reissner inverse-shell element formulation for complex stiffened shell structures, Ocean Eng. 305 (2024) 118028.

[18] E. Del Priore, L. Lampani, A methodology for applying isogeometric inverse finite element method to the shape sensing of stiffened thin-shell structures, Thin-Walled Struct. 199 (2024) 111837.

[19] C. De Mooij, M. Martinez, R. Benedictus, iFEM benchmark problems for solid elements, Smart Mater. Struct. 28 (6) (2019) 065003.

[20] F. Zhao, H. Bao, F. Zhang, Geometrically nonlinear deformation reconstruction of based on Euler–Bernoulli beam theory using a nonlinear iFEM algorithm, Thin-Walled Struct. 189 (2023) 110884.

[21] F. Zhao, Y. Guo, H. Bao, Shape sensing of the thin-walled beam members by coupling an inverse finite element method with a refined quasi-3D zigzag beam theory, Thin-Walled Struct. (2024) 112127.

[22] R. Roy, C. Surace, M. Gherlone, Full-field deformation reconstruction of beams using the inverse finite element method: Application to thin-walled structures, Thin-Walled Struct. 200 (2024) 111907.

[23] A. Kefal, A. Tessler, E. Oterkus, An enhanced inverse finite element method for displacement and stress monitoring of multilayered composite and sandwich structures, Compos. Struct. 179 (2017) 514–540.

[24] I. Khalid, Z.A. Qureshi, H.Q. Ali, S. Oterkus, E. Oterkus, Structural health monitoring of precracked structures using an in-plane inverse crack-tip element, Int. J. Mech. Syst. Dyn. 4 (4) (2024) 406–426.

[25] O. Eugenio, Structural Analysis with the Finite Element Method: Linear Statics, Springer Netherlands, 2009.

[26] J.-L. Batoz, M.B. Tahar, Evaluation of a new quadrilateral thin plate bending element, Internat. J. Numer. Methods Engrg. 18 (11) (1982) 1655–1677.

[27] D. Allman, A compatible triangular element including vertex rotations for plane elasticity analysis, Comput. Struct. 19 (1–2) (1984) 1–8.

[28] M. Abdollahzadeh, H.Q. Ali, M. Yildiz, A. Kefal, Experimental and numerical investigation on large deformation reconstruction of thin laminated composite structures using inverse finite element method, Thin-Walled Struct. 178 (2022) 109485.

[29] D. Allman, A quadrilateral finite element including vertex rotations for plane elasticity analysis, Internat. J. Numer. Methods Engrg. 26 (3) (1988) 717–730.

[30] A. Ibrahimbegovic, R.L. Taylor, E.L. Wilson, A robust quadrilateral membrane finite element with drilling degrees of freedom, Internat. J. Numer. Methods Engrg. 30 (3) (1990) 445–457.

[31] S. Timoshenko, J. Goodier, Theory of elasticity, Inc. New York 1 (1951) 35–39.

[32] T. Belytschko, H. Stolarski, W.K. Liu, N. Carpenter, J.S. Ong, Stress projection for membrane and shear locking in shell finite elements, Comput. Methods Appl. Mech. Engrg. 51 (1–3) (1985) 221–258.